ONSET OF FLOW INSTABILITY IN UNIFORMLY HEATED, NARROW, RECTANGULAR CHANNELS

A Thesis
Presented to
The Academic Faculty

by

Charles Becht V

In Partial Fulfillment
of the Requirements for the Degree
of Masters in Nuclear Engineering in the
School of Mechanical Engineering

Georgia Institute of Technology
August 2006

ONSET OF FLOW INSTABILITY IN UNIFORMLY HEATED, NARROW, RECTANGULAR CHANNELS

Approved by:

Dr. Said I. Abdel-Khalik, Advisor
School of Mechanical Engineering
Georgia Institute of Technology

Dr. S. Mostafa Ghiaasiaan
School of Mechanical Engineering
Georgia Institute of Technology

Dr. Sheldon M. Jeter
School of Mechanical Engineering
Georgia Institute of Technology

Date Approved: April 16th, 2007

ACKNOWLEDGEMENTS

I wish to thank Dr. Said Abdel-Khalik, my advisor throughout the thesis process, for his tireless support and feedback. I also want to thank Dr. Sheldon Jeter for his mentoring throughout my research. Without the support I received from both of them I would not of been able to finish this project. I'd also like to thank Dr. Mostafa Ghiaasiaan for his assistance and comments as a member of my reading committee.

I also wish to thank Dennis Sadowski for helping build and design the components necessary for my experimental setup. His help was integral in creating the test section and its peripheral components.

My mother and father also deserve thanks for without their guidance and support I would have been here. Over the years they have helped shape me and I would not have been able to set and accomplish my goals in life without them.

Finally I wish to thank Lauren Pica for her loving support of all my efforts. Her motivating words helped focus and guide me to the completion of this thesis.

TABLE OF CONTENTS

LIST OF TABLES

LIST OF FIGURES

NOMECLATURE

A	Surface area (m)
c	Speed of sound in gas phase (m/s)
C_p, c_p	Specific heat at constant pressure (J/kg-K)
C_v	Specific heat at constant volume (J/kg-K)
D	Diameter (m)
D_o	Reference diameter (m)
D_h	Hydraulic diameter (m)
f	general friction factor of D`Arcy friction factor
G	Mass flux (kg/m^2-s)
g	Gravitational acceleration (m/s^2)
h	Heat transfer coefficient (W/m^2)
$h_{b,(h20)}$	Heat transfer coefficient for nucleate boiling in stationary water (W / m^2K)
h_k	Heat transfer coefficient for fully developed single-phase flow in an annulus (W/m^2K)
h	Enthalpy (J/kg)
K	Parameter in Petukhov C=correlation
k	Thermal conductivity (W/m-K)
l	Length scale (m)
L	Channel length (m)
LMTD	Log mean temperature difference (K)
Nu	Nusselt number = (hD/k)
P, p	Pressure (Pa)
ΔP, Δp	Differential pressure (Pa)

Pr	Prandtl number
q”	Heat flux (W/ m2)
R	Radius (m)
r	Radial coordinate (m)
Re	Reynolds number
T	Temperature (K, ºC)
U, u	Velocity (m/s)
V, v	Velocity (m/s)
x	Quality

Greek Letters

α	Void fraction (-)
γ	Ratio of ideal gas specific heats – (c_p/c_v)
μ	Dynamic viscosity (kg/m-s)
σ	Standard deviation
υ	Kinematic viscosity (m^2/s)
Φ	Enhancement ratio = (Nu_{exp}/Nu_{Gn})
ρ	Density (kg/m^2)
τ	Shear stress (N/m^2)

SUMMARY

The primary purpose of this investigation was to experimentally determine the effect of operational parameters on the onset of flow instability (OFI) in narrow, uniformly heated, vertical, rectangular channels. The geometry investigated was a 9.0 cm long rectangular channel with a 1.0mm by 1.3cm cross section. This geometry closely matches the coolant channel geometry in an accelerator target. Nitrogen-saturated subcooled water was used as the coolant, with mass fluxes ranging from 250 to 1336 kg/m^2 s, and an inlet temperature of 26ºC for the OFI experiments. The exit pressures investigated ranged from 275kPa to 620kPa, while the heat flux ranged from 0.729 to 2.236 MW/m^2. The primary data collected from these experiments were used to develop two correlations for the heat flux and mass flux at OFI.

$$q''_{OFI} = 0.561 * q''_{sat} \pm 6.41\%$$

$$G_{OFI} = 1.790 * G_{sat} \pm 7.96\%$$

Wall temperature data were also collected in order to develop a Nusselt number correlation for the single-phase regime. This correlation is valid for the Reynolds number range of $6x10^3$ to $1.7x10^4$.

$$Nu_d = 0.0429\,\mathrm{Re}_d^{0.711}\,\mathrm{Pr}^{0.33} \pm 3.036\%$$

The data obtained in this investigation will aid designers of high-power-density systems establish design limits to prevent over heating and possible damage due to the onset of flow instability.

CHAPTER I

INTRODUCTION

Forced convection using single-phase liquid water is a common cooling mechanism in high power density engineering applications. Typically, design specifications require the coolant to remain sub-cooled throughout the heat transfer channel to ensure adequate cooling of the heated surfaces. Despite these planned steady state parameters, accident or transient conditions can cause boiling to take place within the channels. For this reason, it is important in the design and operation of heated channels to understand and predict the onset of boiling and two-phase flow instabilities that can lead to channel dryout and potential overheating and/or burnout of the heat transfer system.

The research presented here deals with experiments that examine the onset of flow instability (OFI) and the heat transfer coefficient in uniformly heated narrow rectangular channels. In this thesis, flow channels and gaps of 1mm clearance are referred to as microchannels. OFI corresponds to the flow rate that produces a minimum pressure difference over the channel length. As explained later, a lower flow rate can yield unstable conditions for which any small fluctuation can cause a large change in the flow rate. This chapter provides a brief description of the OFI phenomena.

1.1 Onset of Flow Instability (OFI)

Figure 1.1 shows a typical demand curve for a uniformly heated channel. In the high mass flux regime, sub-cooled single-phase conditions exist throughout the channel. Consequently, all heat transfer is accomplished through single-phase forced convection. As the mass flux through the channel is decreased, sub-cooled boiling, followed by saturated boiling, and finally single-phase convection to superheated vapor take place (Stoddard, et al., 2000).

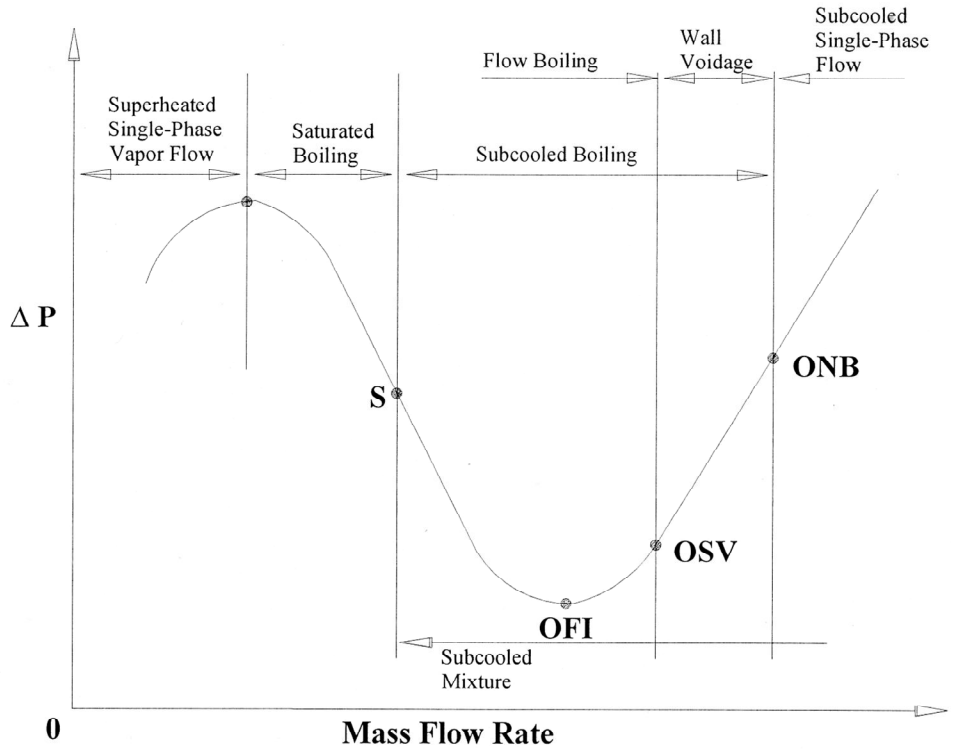

Figure 1.1: Schematic Diagram of the Demand Curve for a Heated Channel with Constant Heat Rate

In Figure 1.1, the terms ONB, OSV, OFI, and S refer to the onset of nucleate boiling, onset of significant void, onset of flow instability, and saturation conditions, respectively.

At mass flow rates higher than the OSV point, the coolant flow is primarily single-phase sub-cooled liquid with some bubbles sticking to the walls of the heated channels. These bubbles are unable to withstand condensation and hence collapse when released from the wall and mix with the bulk fluid flow. At the onset of significant void, the void fraction is typically around five percent, and bubbles released from the channel walls survive condensation and become entrained in the bulk fluid flow; the flow becomes two-phase. Flow boiling exists for mass flow rates below the OSV point value, and a fully developed nucleate boiling regime dominates. For high mass fluxes, the onset of significant void and the initiation of flow boiling occur at approximately the same point. Further decrease of the mass flow rate will eventually result in an increase in the pressure drop because of the pressure required to accelerate the evaporating vapor and because of the wall friction created by the high velocity vapor flow. As the mass flux through the heated channel decreases to the point where the pressure drop across the channel is at a minimum on the demand curve, a situation is created where a flow excursion can result. This part of minimum local pressure drop is called the onset of flow instability (OFI) (Stromberger, 2003).

To understand the possible flow excursion at OFI condition, refer to the demand curve shown in Figure 1.2. Case "A" represents the situation that would exist if a positive displacement pump were used to circulate the coolant through a heated channel (Lahey and Moody, 1979). A positive displacement pump operating at a given speed would force coolant through the boiling channel at a fixed rate regardless of the overall pressure drop. For this reason, the channel could be operated at position "1" by maintaining a constant pump speed. Case "B" represents the situation where numerous

channels operate in parallel with the boiling channel. For this case, operating the system steadily and continuously at position "1" is impossible. A small negative perturbation in the flow rate would immediately shift conditions to position "2" while a small positive perturbation would shift the flow state to position "3". A flow excursion from position "1" to position "2" would result in a significant reduction in flow rate within the heated channel and may lead to dryout or physical burnout of the channel. Case "C" represents the situation that would result if a centrifugal pump with a relatively flat characteristic curve were used to circulate the coolant through the heated channel. Once again, steady and continuous operation at position "1" is impossible since a small perturbation could result in a flow excursion to either position "2`" or position "3`". Finally, Case "D" represents a situation where the circulation pump has a steep characteristic curve so that position "1" could be steadily maintained and Ledinegg instability (Todrease and Kazimi, 1990) would not occur (Stromberger, 2003).

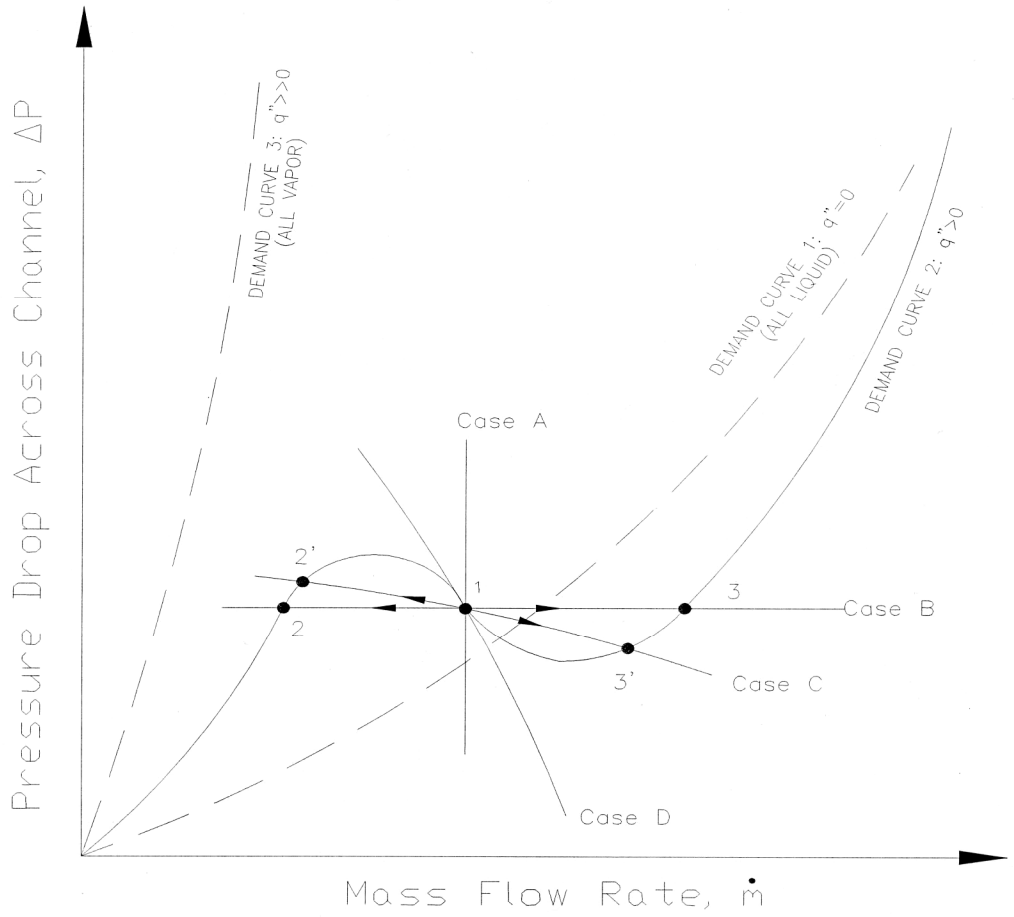

Figure 1.2: Excursive Instability (from Lahey and Moody, 1979)

In order to prevent Ledinegg flow excursions in practical systems, limits are imposed on the channel power input to exclude the possibility of operation within the negative-sloped segment of the demand curve at all anticipated flow rates. Typically, these power limits are conservatively estimated by using OSV models and/or correlations. OSV is considered a precursor to the onset of flow instability (OFI), which in turn, may be viewed as a precursor to the critical heat flux (CHF). Several investigations have been conducted at Georgia Tech (Kennedy, et al., 1997; Roach, et al.,

1998; Blasik, et al., 1999; Stoddard, et al., 2000; stromberger, et al., 2003) to quantify the effects of channel geometry and operating conditions on OFI for uniformly-heated microchannels. This investigation builds on the results of these earlier studies by examining the differences associated with rectangular shaped microchannels. Such geometry is used widely in industry, and therefore represents significant work. The difference in geometry may impact the vapor bubble dynamics within the channel, and hence, the demand curve and OFI point.

1.2 Motivation and Objectives

As a result of the potentially severe consequences of Ledinegg flow excursion and critical heat flux, several experimental and theoretical studies have been performed to quantify the effect of various design and operation parameters on these limits. The existing experimental data and correlations are well established for channels with hydraulic diameters larger than 4 mm. The database was recently extended to include smaller diameter channels with hydraulic diameters in the order of 1mm. The majority of these investigations were performed at Georgia Tech (Kennedy, et al., 1997; Roach, et al., 1998; Blasik, et al., 1999; Stoddard, et al., 2000; stromberger, et al., 2003). This investigation builds on the earlier work performed at Georgia Tech by examining narrow rectangular cross-sections, as opposed to the annular cross-sections of all the previous experiments. The change in OFI conditions were studied along with the single-phase forced convection coefficient.

The experiments conducted in this investigation provide designers of high-power density systems cooled by forced convection in microchannels with the necessary data to establish the thermal safety limits for such systems under realistic operational conditions.

The remainder of this thesis is organized as follows. Chapter II provides a brief overview of the literature available on OFI, CHF, single-phase forced convection, flow boiling and fluid-structure interaction in small diameter channels. Chapter III gives a detailed description of the instrumentation and equipment used in all experiments performed during this investigation. Chapter IV outlines the experimental procedures used to setup and perform OFI and single-phase forced convection experiments investigating the rectangular cross-section. All OFI and forced convection experimental results are reported and compared with available models in Chapter V. Finally, Chapter VI summarizes the conclusions of this investigation and provides recommendations for future microchannel heat transfer research.

CHAPTER II

LITERATURE REVIEW

2.1 Introduction

Two phase flow instability can lead to serious safety problems in the operation of heated channels supporting forced and natural circulatory flow. For this reason, it is important in the design of heated channels to understand and predict the onset of boiling and two phase flow instabilities that can lead to channel dryout and potential overheating of the heat transfer system. Reviews of flow instability and critical heat flux have been published by McBeth, *et al.* (1964)*;* Bowring (1972); Boure, *et al.* (1973); Ishii (1976); Bergles (1977); Yadigaroglu (1981); Groenenveld, *et al.* (1986); Bankoff, *et al.* (1991); and Caira, *et al.* (1993). More recently, a comprehensive review of two-phase phenomena in microchannels was published by ghiaasiaan and Abdel-Khalik (2001). Correlations and findings on single-phase forced convection have been extracted from literature by petukhov, *et al.* (1970), Gnielinski (1976), Incropera and De Witt (1990), Todreas and Kazimi (1990), Wagner (1998). The following is a brief overview of previous work on OFI and single-phase forced convection.

2.2 Onsent of Flow Instability (OFI)

Two phase flow instabilities are generally categorized as either dynamic or static (Boure, *et al.*, 1973). Dynamic instabilities (e.g.,flow regime oscillations) involve transient inertial dynamic and feedback effects and lead to oscillary flows, which can be analyzed using the transient flow conservation equations. Modeling system behavior during dynamic oscillations, however, requires numerical solution of nonlinear conservation equations when perturbations are imposed on the flow (Gurgenci, *et al.*, 1983). Dynamic instabilities occur over a broad range of conditions and become serious safety problems when their amplitudes become large.

Static instabilities result from pressure drop versus flow rate characteristics of heated channels and can be analyzed using steady state flow conservation equations. The typical demand curve (*i.e.* plot of steady state pressure drop versus flow rate) of a boiling channel has an inverted S-shape. The different two-phase flow regimes for heated channels are shown in Figure 1.3. As described in Chapter I, when the channel is part of a forced circulation loop, the segment of the demand curve with negative slope can be unstable depending on pump characteristics. If the mass flow rate through the channel drops below the local minimum point on the curve, then a flow excursion can occur resulting in a significant reduction in the flow rate through the channel. Such flow excursions can lead to physical burnout of the heated channel.

The onset of flow instability (OFI) is normally expected to occur at a slightly lower flow rate than the flow rate corresponding to the onset of significant void. The onset of significant void (OSV) occurs when a further reduction in flow rate results in a sharp increase in coolant void fraction in the channel. Consequently, at a slightly lower

flow rate the pressure drop due to flow acceleration resulting from increased voidage will render the gradient of the demand curve negative. OSV can therefore be considered a conservative criterion for avoiding classic Ledinegg flow excursions (Yadigaroglu, 1981). Furthermore, OSV signifies the initiation of flow boiling in the subcooled flow-boiling regime. The OSV condition may be of special importance to other processes in a heat transfer system; for example, if significant voiding develops in a nuclear reactor, the reactor power may be affected by reactivity feedback (Kennedy, *et al.*, 1997).

In the past, OSV and void fraction have been extensively studied in channels experiencing subcooled boiling (Whittle and Forgan, 1967; Evangelisti and Lupoli, 1969; Chan, 1984; Rogers, *et al.*, 1987; Johnston, 1989;Ahmad, 1970; Dix, 1971; Levy, 1967; Staub, 1968; Unal, 1975). Most of the published studies, however, deal with OSV and OFI in relatively large channels. Only recent work performed at Georgia Tech (Kennedy, *et al.*, 1997; Roach, *et al.*, 1998; Blasick, *et al.*, 1999; Stoddard, *et al.*, 2000; Ghiaasiaan and Abdel-Khalik, 2001) addresses channel designs of smaller hydraulic diameters.

OSV, OFI, and other related phenomena occur where flow channels typically have small hydraulic diameters, e.g. research reactors and computer chips. However, systematic studies dealing with OSV and OFI in microchannels are scarce. Inasaka, *et al.* (1989) measured subcooled boiling pressure drop in channels with diameter 1.0 mm and larger. They noted that the onset of nucleate boiling (ONB) point was well predicted by the correlation of Bergles and Rhosenow (1964), while the correlations of Saha and Zuber (1974) and Levy (1967) both failed to predict OSV data well in small channels. Their measured two-phase friction factor multipliers for capillaries, however, were considerably smaller than the values predicted by the Lockhart and Martinelli (1949)

correlation. Inasaka, *et al.* (1989) attribute the latter discrepancy to the possible overprediction of quality in capillaries by Ahmad's correlation (Ahmad, 1970). Hainoun, *et al.* (1996) recently reported a two fluid model capable of predicting OFI phenomenon in small channels. Their model applies the correlation of Saha and Zuber (1974) for the prediction of OSV. The aforementioned correlations are only applicable under limited conditions and do not accommodate practical insufficiencies of the cooling systems or any perturbation. In this investigation, experiments have been conducted that focus on rectangular channels.

2.2.1 Flow Instability Initiation

During a hypothetical loss of coolant accident in a reactor, the coolant flow rate through the heated channels decreases. Under normal operating conditions, the coolant remains subcooled and thus single-phase. However, if a substantial drop in flow rate occurs, the onset of nucleate boiling (ONB) may be reached. Bankoff, *et al.* (1991) presented a comprehensive review of ONB and the mechanics of bubble formation and departure. At the ONB point, bubbles begin to form on the walls of the heated channel Due to the subcooled status of the bulk coolant, these bubbles either collapse or slide along the channels walls; they do not separate and survive in the bulk flow. The presence of the bubbles on the walls causes the differential pressure across the test section to increase. In turn, the friction factor rises due to the increased differential pressure across the channel. When vapor generation becomes great enough, the bubbles detach from the walls and survive in the subcooled, bulk coolant flow. This situation is defined as OSV in the previous chapter. Vapor bubbles in the bulk flow act to lower the average density

of the fluid within the channel. The increased apparent friction factor coupled with the increased acceleration term causes the differential pressure across the channel to rise. In parallel channels with an imposed external pressure difference, the flow can easily become unstable and possibly dry out due to a flow excursion (Bankoff, *et al.*, 1991; Lahey and Moody, 1979).

2.2.2 Onset of Significant Void (OSV)

Many models and correlations exist which predict OSV. Some of these models are based on theoretical arguments while others are based on empirical analysis. In general, two phase flow phenomena are difficult to model theoretically which explains the development and use of empirical correlations. Examples of commonly accepted formulations include those reported by Bowring (1962), Saha and Zuber (1974), and Unal (1975). Some correlations such as Levy (1967), Staub (1968), and Rogers, *et al*. (1987) incorporate a theoretical model with empirical adjustments. Bankoff, *et al.* (1991), reported a comprehensive review of the subject. The more widely reported correlations and recent OFI correlations produced at Georgia Tech by Kennedy, *et al.* (1997), Roach (1998), Blasick (1999) and Stoddard (2000) in conjunction with the Accelerator Production of Tritium (APT) project are summarized in Table 2.1 to 2.13.

Theoretical OSV models are based on vapor bubble mechanics in vertical, upward, subcooled flow. The mechanics involved in analyzing bubble behavior focus on the heat transfer and fluid flow at the bubble-liquid interface. Bubble departure is determined by performing a force balance. Three aspects of the bubble-liquid interface combine to determine when the bubble will depart the channel wall: buoyancy of the

bubble within the liquid, shear force exerted on the bubble by the flowing liquid, and the surface tension which holds the bubble to the wall.

Of the three OSV correlations described by Bankoff, *et al.* (1991), the one proposed by Levy (1967) is the simplest. The levy correlation is valid for water under the following conditions: mass flux range of 130 to 1420 kg/m^{2}s, operating pressure between 0.41 and 13.6 MPa, and heat flux from 0.24 to 1.91 MW/m^2.

The model of Staub (1968) is applicable for two channel geometries: circular with hydraulic diameter between 6 and 200 mm and rectangular with hydraulic diameter between 4 and 66 mm. The correlation is valid for both water and R-22, but no range is specified for the applicable heat fluxes.

The correlation of Rogers, *et al.* (1987) is more specific and therefore more restricted than those of Levy and Staub. This correlation is only valid for annular tube geometry with three specific hydraulic diameters: 9 mm, 12 mm and 17 mm. Also, this correlation only holds for tube lengths of 480 and 600 mm. This correlation is valid for water under the following conditions: mass flux range of 70 to 450 kg/m^{2}s, operating pressure between 1.50 and 1.55 Mpa, and heat flux from 0.3 to 1.2 MW/m^2.

Even though the analytical models of OSV are similar, it is interesting to note that different bubble shapes are assumed. Levy assumed a spherical shaped bubble, Staub assumed a hemispherical bubble that took on the contour of the channel, and Rogers, *et al.* assume that the bubble was a truncated sphere, with a contact angle at the surface equal to the equilibrium contact angle (Bankoff, 1991).

Often it is easier to use empirical correlations as opposed to theoretical models for OSV prediction due to the complex mechanisms that exist in two-phase flow. Several

empirical models are summarized in Stoddard (2000). However, for each of these correlations, the liquid subcooling at the OSV point can be expressed as a function of pressure, hydraulic diameter, heated length, heat flux, mass flux, inlet temperature, and fluid properties at designated temperature and pressure. For example, a pressure term is used in the Bowring (1962) correlation while other correlations only consider the effect of pressure on fluid properties. It is also interesting to note that Bowring (1962) and Thom, *et al.* (1966) are the only dimensional correlations; Saha and Zuber (1974), Unal (1975), Ahmad (1970), and Sekoguchi, *et al.* (1974) are all dimensionless. In fact, the Saha and Zuber (1974) correlation includes both the Stanton and Nusselt numbers. This signifies that under low mass flux conditions, flow behavior is hydrodynamically controlled. The Unal (1975) correlation suggests a similar split into two different regimes that depend on flow velocity.

The theoretical models described above have been compared with the empirical models. Both the theoretical Levy (1967) correlation and the empirical Bowring (1962) correlation predict that as liquid flow rate through the channel increases, the degree of subcooling at the OSV point decreases. Similarly, the theoretical Staub (1968) correlation was compared with the empirical models of Costa (1967), Griffith, *et al.* (1968), Christensen (1961), and Kroeger and Zuber (1968). The experimental data as compared to the predictions of the Staub (1968) correlation were 15% higher for circular channels and 15% lower for rectangular channels.

Table 2.1: Theoretical OSV Model (1967) by Levy

Features

Author:	Levy (1967)
Model Type:	Theoretical, Dimensionless
Tube Shape:	No Restriction
Tube Diameter:	No Restriction
Tube Length:	No Restriction
Tube Orientation:	Vertical
Flow Direction:	Upwards
Medium:	Water
Mass Flux:	130 to 1420 kg/m^2•s
Pressure:	0.41 to 13.6 MPa
Heat Flux:	0.24 to 1.91 MW/m^2

Formulation

Dimensional Distance to Tip of Bubble:

$$Y_B^+ = 0.015 \frac{\sqrt{\sigma \cdot D_h \cdot \rho_f}}{\mu_f}$$

Heat Transfer Coefficient:

$$h = 0.023 \frac{k_f}{D_h} \mathrm{Re}_f^{0.8} \cdot \mathrm{Pr}_f^{0.4}$$

Wall Shear and Friction Factor:

$$\tau_w = \frac{f}{8} \rho_f \cdot V_f^2$$

$$f = 0.0055 \left[1 + \left(20{,}000 \frac{\varepsilon}{D_h} + \frac{10^6}{\mathrm{Re}_f} \right)^{1/3} \right]$$

$$\frac{\varepsilon}{D_h} = 10^{-4}$$

Table 2.1 (continued)

Heat Flux Parameter:

$$Q = \frac{q''}{\rho_f \cdot C_{pf} \cdot \sqrt{\frac{\tau_w}{\rho_f}}}$$

Conditions for Onset of Bubble Departure:

$0 < Y_B^+ < 5$	$T_s - T_{f,d} = \frac{q''}{h} - Q \cdot Pr_f \cdot Y_B^+$
$5 < Y_B^+ < 30$	$T_s - T_{f,d} = \frac{q''}{h} - 5 \cdot Q \left\{ Pr_f + \ln\left[1 + Pr_f \left(\frac{Y_B^+}{5} - 1 \right) \right] \right\}$
$Y_B^+ > 30$	$T_s - T_{f,d} = \frac{q''}{h} - 5 \cdot Q \left\{ Pr_f + \ln\left[1 + Pr_f \right] + 0.5 \cdot \ln\left[\frac{Y_B^+}{30} \right] \right\}$

Table 2.2: Theoretical OSV Model (1968) by Staub

Features

Author:	Staub (1968)
Model Type:	Theoretical, Dimensionless
Tube Shape:	Circular, Rectangular
Tube Diameter:	0.006 to 0.020 m, 0.004 to 0.066 m
Tube Length:	Unknown
Tube Orientation:	Vertical
Flow Direction:	Upwards
Medium:	Water, R-22
Flow Rate:	0.5 to 8.0 m/s, 0.1 to 0.9 m/s
Pressure:	0.17 to 6.8 MPa
Heat Flux:	Unknown

Formulation

Bubble Diameter:

$$\frac{f \cdot \rho_f \cdot V_f^2 \cdot D_B}{32 \cdot g \cdot \sigma \cdot f(\beta)} + \frac{D_B^2 (\rho_f - \rho_g)}{12 \cdot \sigma \cdot f(\beta)} = 1.0 \text{ Engineering Units}$$

$$f(\beta) = 0.02 \quad \text{for } V_f < 0.45 \text{ (m/s)}$$
$$f(\beta) = 0.03 \quad \text{for } V_f > 0.45 \text{ (m/s)}$$

Dimensionless Distance to Tip of Bubble:

$$Y_B^+ = 0.5 \cdot D_B \frac{\rho_f \cdot V_f \sqrt{\frac{f}{8}}}{\mu_f}$$

Wall Shear and Friction Factor:

$$f = \frac{8 \cdot \tau_w}{\rho_f \cdot V_f^2} = f \cdot \left(\mathrm{Re}_f \frac{D_B}{2 \cdot D} \right)$$

Table 2.2 (continued)

Conditions for Initial Point of Net Vapor Generation (IPNVG):

$0 < Y_B^+ < 5$

$$T_s - T_{f,d} = Q\left\{\mathrm{Pr_f}\left(5 - Y_B^+\right) + 5 \cdot \ln\left(1 + 5\,\mathrm{Pr_f}\right) + 2.5\left[\frac{\ln Y_C^+ / 30}{1 - 30/Y_C^+} - 1\right]\right\}$$

$5 < Y_B^+ < 30$

$$T_s - T_{f,d} = Q\left\{5 \cdot \ln\left[\frac{1 + 5\,\mathrm{Pr_f}}{1 + \mathrm{Pr_f}\left(Y_B^+/5 - 1\right)}\right] + 2.5\left[\frac{\ln Y_C^+ / 30}{1 - 30/Y_C^+} - 1\right]\right\}$$

$Y_B^+ > 30$

$$T_s - T_{f,d} = 2.5 \cdot Q\left[\frac{\ln Y_C^+ / Y_B^+}{1 - Y_B^+/Y_C^+} - 1\right]\left(1 - Y_B^+/Y_C^+\right)$$

Where:

$$Y_C^+ = \frac{D}{2}\frac{\rho_f \cdot V_f\sqrt{\frac{f}{8}}}{\mu_f}$$

$$Q = \frac{q''}{C_{pf} \cdot \rho_f \cdot V_f\sqrt{\frac{f}{8}}}$$

Table 2.3: Theoretical OSV Model (1987) by Roger, *et al.*

Features

Author:	Rogers, et al. (1987)
Model Type:	Theoretical, Dimensionless
Tube Shape:	Annulus
Tube Diameter:	D_h = 0.009, 0.0012, 0.0017 m
Tube Length:	0.48, 0.60 m
Tube Orientation:	Vertical
Flow Direction:	Upwards
Medium:	Water
Mass Flux:	70 to 450 kg/m^2•s
Pressure:	1.50 to 1.55 MPa
Heat Flux:	0.3 to 1.2 MW/m^2

Formulation

Dimensionless Distance to Tip of Bubble:

$$Y_B^+ = \frac{\rho_f}{\mu_f}\sqrt{\frac{\tau_w}{\rho_f}}\left(1+\cos\theta_0\right)\left[\frac{3}{4\pi}\cdot\frac{c_2}{c_1}\cdot\frac{C_d\cdot\mu_f^2}{g}\right]\lambda$$

Where:

$$\lambda = \left[1+\frac{8\cdot\pi^2}{3}\frac{c_1\cdot c_2\cdot c_s\cdot g\cdot\sigma}{c_2^2\cdot C_d^2\cdot\rho_f\cdot u_r^4}\right]^{0.5} - 1$$

$$c_1 = 2+3\cos\theta_0-\cos^3\theta_0$$

$$c_2 = \pi-\theta_0+\cos\theta_0\sin\theta_0$$

$$c_3 = \sin\theta_0\left[\cos(\theta_0-10)-\cos(\theta_0+10)\right]$$

$$c_s = \frac{58}{\theta_0+5}+0.14$$

$$C_d = 1.22 \qquad \text{for } 20 < Re_B < 40$$

$$C_d = \frac{24}{\mathrm{Re}_B} \qquad \text{for } 4 < Re_B < 20$$

Table 2.3 (continued)

$$\mathrm{Re}_B = \frac{\rho_\mathrm{f} \cdot u_r (2 \cdot r_B)}{\mu_\mathrm{f}}$$

Calculation of u_r:

$$Y_r^+ = 0.5 \cdot Y_B^+ (1 + \cos\theta_0)$$

$Y_r^+ < 5.0$	$u_r^+ = Y_r^+$
$5.0 < Y_r^+ < 30$	$u_t^+ = 5.0 \cdot \ln Y_r^+ - 3.08$
$Y_r^+ > 30$	$u_r^+ \cdot 2.5 \cdot \ln Y_r^+ + 5.5$

Wall Shear and Friction Factor:

$$f = \frac{8 \cdot \tau_w}{\rho_\mathrm{f} \cdot V_\mathrm{f}^2} = 0.046 \cdot \mathrm{Re}^{-0.20}$$

Calculation of T_B^+:

$Y_B^+ < 5.0$	$T_B^+ = \mathrm{Pr}_\mathrm{f} \cdot Y_B^+$
$5.0 < Y_B^+ < 30$	$T_B^+ = 5\left[\mathrm{Pr}_\mathrm{f} + \ln\left\{1 + \mathrm{Pr}_\mathrm{f}\left(\frac{Y_B^+}{5} - 1\right)\right\}\right]$
$Y_B^+ > 30$	$T_B^+ = 5\left[\mathrm{Pr}_\mathrm{f} + \ln(1 + 5\,\mathrm{Pr}_\mathrm{f}) + 5.0 \cdot \ln\left(\frac{Y_B^+}{30} - 1\right)\right]$

Conditions for OSV:

$$T_\mathrm{s} - T_\mathrm{f,d} = q''\left[\frac{1}{F_R \cdot h} - \frac{T_B^+}{C_\mathrm{pf} \cdot \rho_\mathrm{f}\sqrt{\frac{\tau_w}{\rho_\mathrm{f}}}}\right]$$

Where:

$$Nu = 0.023 \cdot \mathrm{Re}_\mathrm{f}^{0.8} \cdot \mathrm{Pr}_\mathrm{f}^{0.4}$$

$$F_R = 1.11 + -0.036 \quad \text{for } \theta_0 = 30°$$

$$F_R = 1.06 + -0.022 \quad \text{for } \theta_0 = 80°$$

Table 2.4: Empirical OSV Correlation (1962) by Bowring

Features

Author:	Bowring (1962)
Model Type:	Empirical, Dimensional
Tube Shape:	Unknown
Tube Diameter:	Unknown
Tube Length:	Unknown
Tube Orientation:	Unknown
Flow Direction:	Unknown
Medium:	Water
Mass Flux:	Unknown
Pressure:	1.1 to 13.8 MPa
Heat Flux:	Unknown

Formulation

$$T_s - T_{f,d} = \eta \frac{q''}{V_f}$$

Where: $$\eta = 10^{-6}\left(14.0 + P\right)$$

Table 2.5: Empirical OSV Correlation (1966) by Thom, *et al.*

Features

Author:	Thom, *et al.* (1966)
Model Type:	Empirical, Dimensional
Tube Shape:	Unknown
Tube Diameter:	Unknown
Tube Length:	Unknown
Tube Orientation:	Vertical
Flow Direction:	Upwards
Medium:	Water
Mass Flux:	Unknown
Pressure:	5.14 to 6.80 MPa
Heat Flux:	Unknown

Formulation

$$T_s - T_{f,d} = 0.02 \cdot h_{fs} \frac{q''}{G \cdot h_{fg}}$$

Table 2.6: Empirical OSV Correlation (1970) by Ahmad

Features

Author:	Ahmad (1970)
Model Type:	Empirical, Dimensionless
Tube Shape:	Circular, Rectangular
Tube Diameter:	0.004 to 0.007 m
Tube Length:	Unknown
Tube Orientation:	Vertical
Flow Direction:	Upwards
Medium:	Water
Mass Flux:	Less than 8000 kg/m^2•s
Pressure:	0.17 to 0.5 MPa, 8.3 and 11.0 MPa
Heat Flux:	Unknown

Formulation

$$T_s - T_{f,d} = \frac{q''}{h}$$

$$h = 2.44 \frac{k_f}{D_h} \mathrm{Re}_f^{0.5} \cdot \mathrm{Pr}_f^{1/3} \left(\frac{h_{fi}}{h_{fs}} \right)^{1/3} \left(\frac{h_{fg}}{h_{fs}} \right)^{1/3}$$

Table 2.7: Empirical OSV Correlation (1971) by Dix

Features

Author:	Dix (1971)
Model Type:	Empirical, Dimensionless
Tube Shape:	Annulus
Tube Diameter:	0.018 m
Tube Length:	1.07 m
Tube Orientation:	Vertical
Flow Direction:	Upwards
Medium:	R-114
Mass Flux:	100 to 210 kg/m^2•s
Pressure:	0.32 and 0.85 MPa
Heat Flux:	0.004 to 0.03 MW/m^2

Formulation

$$T_s - T_{f,d} = 0.00135 \frac{q''}{h} \mathrm{Re}_f^{1/2}$$

Table 2.8: Empirical OSV Correlation (1974) by Saha and Zuber

Features

Author:	Saha and Zuber (1974)
Model Type:	Empirical, Dimensionless
Tube Shape:	Circular, Rectangular, Annulus
Tube Diameter:	0.01 to 0.24 m, 0.004 to 0.012 m, 0.012 to 0.026 m
Tube Length:	Unknown
Tube Orientation:	No Restriction
Flow Direction:	No Restriction
Medium:	Water, R-22, R-114
Mass Flux:	Unknown
Pressure:	0.1 to 13.8 MPa, 1.1 to 13.8 MPa, 0.32, 0.85 MPa
Heat Flux:	Unknown

Formulation

$$Nu = \frac{q'' \cdot D_h}{k_f \left(T_s - T_{f,d}\right)} = 455 \qquad \text{for } Pe \leq 70{,}000$$

$$St = \frac{q''}{G \cdot C_{pf} \left(T_s - T_{f,d}\right)} = 0.0065 \qquad \text{for } Pe > 70{,}000$$

Where:

$$Pe = \frac{Nu}{St} = \mathrm{Re} \cdot \mathrm{Pr} = \frac{G \cdot D_h \cdot C_{pf}}{k_f}$$

Table 2.9: Empirical OSV Correlation (1974) by Sekoguchi, *et al.*

Features

Author:	Sekoguchi, *et al.* (1974)
Model Type:	Empirical, Dimensionless
Tube Shape:	Annulus
Tube Diameter:	0.002 to 0.003 m
Tube Length:	0.7 to 4.5 m
Tube Orientation:	Vertical
Flow Direction:	Upwards
Medium:	Water
Mass Flux:	310 to 2100 kg/m^2•s
Pressure:	0.14 to 1.6 MPa
Heat Flux:	0.05 to 1.75 MW/m^2

Formulation

$$T_s - T_{f,d} = 13.5 \frac{h_{fg}}{C_{pf}} \left(\frac{q''}{h_{fg} \cdot G} \right)^{0.65}$$

Table 2.10: Empirical OSV Correlation (1975) by Unal

Features

Author:	Unal (1975)
Model Type:	Empirical, Dimensionless
Tube Shape:	Circular, Rectangular, Annulus
Tube Diameter:	0.004 to 0.020 m
Tube Length:	Unknown
Tube Orientation:	No Restriction
Flow Direction:	No Restriction
Medium:	Water, R-22
Mass Flux:	132 to 2818 kg/m^2•s, 180 to 1391 kg/m^2•s
Pressure:	0.1 to 15.8 MPa, 1.2 and 3.3 MPa
Heat Flux:	0.15 to 1.92 MW/m^2, 0.02 to 0.06 MW/m^2

Formulation

$$\frac{h\left(T_s - T_{f,d}\right)}{q''} = a \qquad (a = \text{constant})$$

For Water: $a = 0.24$ ($V_f > 0.45$ m/s)
$a = 0.11$ ($V_f < 0.45$ m/s)

For R-22: $a = 0.18$ ($V_f > 0.45$ m/s)
$a = 0.11$ ($V_f < 0.45$ m/s)

Heat Transfer Coefficient:

$$\frac{h \cdot D_h}{k_f} = 0.023 \cdot \mathrm{Re}_f^{0.8} \cdot \mathrm{Pr}_f^{0.4} \qquad \text{for circular and rectangular tubes}$$

$$\frac{h \cdot D_h}{k_f} = 0.020 \left(\frac{D_o}{D_i}\right)^{0.53} \mathrm{Re}_f^{0.8} \cdot \mathrm{Pr}_f^{0.4} \qquad \text{for annulus}$$

Table 2.11: Empirical OFI Correlation (1997) by Kennedy, *et al.*

Features

Author:	Kennedy, *et al.* (1997)
Model Type:	Empirical
Tube Shape:	Circular and Prototypical
Tube Diameter:	1.131 to 1.445 mm
Tube Length:	0.16 m
Tube Orientation:	Horizontal
Medium:	Water
Mass Flux:	800 to 4500 $kg/m^2 \bullet s$
Pressure:	0.344 to 1.034 MPa
Heat Flux:	1.0 to 4.0 MW/m^2

Formulation

$$\left(\Delta T_{\text{subcooling}}\right)_{\text{OFI}} = 10.0 \pm 8.7°\text{C}$$

$$q''_{\text{OFI}} = 0.90 \cdot q''_{\text{sat}} \pm 6.9\%$$

$$G_{\text{OFI}} = 1.11 \cdot G_{\text{sat}} \pm 6.3\%$$

Table 2.12: Empirical OFI Correlation (1998) by Roach

Features

Author:	Roach (1998)
Model Type:	Empirical
Tube Shape:	Prototypical
Tube Diameter:	1.131 to 1.445 mm
Tube Length:	0.16 m
Tube Orientation:	Horizontal
Medium:	Water
Mass Flux:	125 to 950 kg/m^2•s
Pressure:	0.344 to 1.034 MPa
Heat Flux:	0.1 to 0.5 MW/m^2

Formulation

Fully-Degassed:

$$q''_{OFI} = 1.1 \cdot q''_{sat} \pm 10\%$$

$$G_{OFI} = 0.89 \cdot G_{sat} \pm 10\%$$

Air-Saturated:

$$q''_{OFI} = 1.07 \cdot q''_{sat} \pm 10\%$$

$$G_{OFI} = 0.91 \cdot G_{sat} \pm 10\%$$

Table 2.13: Empirical OFI Correlation (1999) by Blasick

Features

Author:	Blasick (1999)
Model Type:	Empirical
Tube Shape:	Annulus
Tube Diameter:	1.448 to 2.002 mm
Tube Length:	0.19 m
Tube Orientation:	Horizontal
Medium:	Water
Mass Flux:	85 to 1428 $kg/m^2 \bullet s$
Pressure:	0.344 to 1.034 MPa
Heat Flux:	0.124 to 1.0 MW/m^2

Formulation

$$q''_{OFI} = 0.900 \cdot q''_{sat} \pm 11.3\%$$

$$G_{OFI} = 1.086 \cdot G_{sat} \pm 9.90\%$$

Table 2.14: Empirical OFI Correlation (2000) by Stoddard

Features

Author:	Stoddard (2000)
Model Type:	Empirical
Coolant Ch. Geometry:	Annulus
Coolant Ch. Gap Thickness:	0.660 to 1.001 mm
Tube Length:	0.19 m
Tube Orientation:	Horizontal
Medium:	Water
Mass Flux:	85 to 2900 kg/m^2 sec
Pressure:	0.344 to 1.034 MPa
Heat Flux:	0.125 to 2.4 MW/m^2

Formulation

$$q''_{OFI} = 0.942 * q''_{sat} \pm 9.80\%$$

$$G_{OFI} = 1.064 * G_{sat} \pm 11.55\%$$

2.3 Single-Phase Forced Convection in Microchannels

The most relevant single-phase forced convection models for turbulent flow published in the literature are summarized Table 2.16. Listing of these correlations and their ranges of applicability may be found in Incropera and De Witt (1990), Todreas and Kazimi (1990), Wagner (1998) and Adams (1999).

Table 2.15: Forced Convection Studies in Microchannels

Study	Transport Variable	Geometry	Gap/Diameter
Levy *et al.* (1959)	Heat	Rectangular	2.54 mm
Lancet (1959)	Momentum/Heat	Rectangular	0.59-0.64 mm
Gambill (1961)	Momentum/Heat	Rectangular	1.09-1.45 mm
Bergles (1962)	Heat	Circular	2.4 mm
Wu and Little (1984)	Momentum/Heat	Trapezoidal	0.134-0.164 mm
Acosta (1985)	Momentum/Mass	Rectangular	0.38,0.96 mm
Nayak *et al.* (1987)	Heat	Rect. Fins	1.0 mm
Choi *et al.* (1991)	Momentum/Heat	Circular	0.003-0.082 mm
Wang and Peng (1994)	Heat	Rectangular	0.311-0.747 mm
Yu *et al.* (1995)	Momentum/Heat	Circular	0.019-0.102 mm
Peng *et al.* (1995)	Heat	Rectangular	0.311-0.646 mm
Peng and Peterson (1996)	Momentum/Heat	Rectangular	0.311-0.367 mm
Adams (1999)	Heat	Circular	0.76-1.13 mm

The use of standard heat transfer correlations for forced convection does not match with current understanding of flow dynamic and heat transfer in microchannels. Adams (1999) discussed in detail the differences between forced convection in microchannels and larger channels.

It has generally been assumed that the well understood turbulent boundary layer characteristics on flat plates apply to the flow field adjacent to the walls of large channels in internal flow. This assumption may be erroneous for microchannels. Schlichting (1968) and Hintze (1975) point out that in a small pipe the buffer zone, the most active

part of the boundary layer with respect to production and dissipation of turbulence may exceed the channel dimensions and therefore could not develop. Thus, the turbulent transport mechanisms of microchannel flow may be phenomenologically different than for flat plates or large channels. Other researchers, Bejan (1984), point out that the use of general forced convection heat transfer correlations on microchannel flow would be inappropriate. He argues that the transition to turbulence is accompanied by an intrinsic turbulent wavelength. This wavelength represents the size of the small eddies, which characterize turbulent circulation and are necessary for its effective initiation and support. The wavelength phenomenon suggests, however, that a lower limit in size of eddies could well hinder the transition to turbulent or its resulting intensity if the size of the passage is on the order of this limit. Generally, the existence of a limitation on eddy size may suppress the mechanism of turbulent heat transfer in narrow channels. Based on this consideration many researchers recommend against applying internal flow and heat transfer correlations for channels with hydraulic diameters less than about 2mm. In such tubes, the turbulent eddy mechanism for fluid flow and heat transfer may be suppressed by the physical size of the tube cross section resulting in lower friction factors and heat transfer coefficients.

A small number of investigators have looked at turbulent convection in narrow passages. Levy *et al.* (1959) conducted experiments on turbulent forced convection of water in rectangular channels measuring 0.1 x 2.5 in (2.54 x 63.5 mm). Over a range of Reynolds numbers from 10^4 to 10^5, their data fell 30 to 50% below values of the heat transfer coefficient predicted by the Sieder-Tate relation.

Gambill and Bundy (1961) studied friction, heat transfer, and burnout for water in turbulent forced convection in thin rectangular channels. Their experiments included flow gaps ranging from 1.09 to 1.45 mm and Reynolds numbers from 9000 to 270,000. Hydraulic diameters ranged from 1.91 to 2.67 mm. The friction factors they obtained were in reasonably good agreement with the Moody chart for the relative roughness of the test sections, and the heat transfer coefficients were actually slightly higher than values predicted by the Sieder-Tate correlation, rejecting the earlier results obtained by Levy.

In an investigation on the effect of a large temperature difference on the turbulent forced convection of water, Bergles and Rohsenow (1962) utilized channels with an inner diameter of 2.4 mm in their test section. They showed that traditional correlations for the heat transfer coefficient were sufficient. However, it should be noted that their investigation aimed to determine the effect of a high temperature difference, not diameter, on forced convection. Furthermore, the channel diameter they used was slightly higher than the diameter limit for which the previous reservations were expressed.

Wu and Little (1984) measured friction factors and heat transfer coefficients of nitrogen gas flowing in trapezoidal channels with hydraulic diameters ranging from 134 to 164 microns with Reynolds numbers less than 2×10^4. They found both increased friction factors and enhanced heat transfer. Furthermore, the difference between the experimental Nusselt numbers and those predicted by the Dittus-Boelter equation increased with increasing Reynolds number, suggesting that the Reynolds analogy does not apply in this case. These effects were attributed to the large asymmetric roughness

which resulted from the abrasive etching processes used to manufacture the channels, effecting large relative roughness in the microchannels.

Other investigators have utilized turbulent convection in rectangular microchannels for the purposes of microelectronic heat sinks, either in theoretical models or actual experiments. The experimental work aimed to verify theoretical models developed for these sinks. However, most of these experiments used large scale test sections rather than actual scale models for increased manufacturing ease. Furthermore, the standard heat transfer correlations used in these studies were cited as one of the main sources of error between theory and experiment. Phillips (1990) gives an excellent review of this work in which he calls for improved turbulent correlations for small channels, especially for lower Reynolds numbers.

Choi *et al.* (1991) measured friction factors and heat transfer coefficients for nitrogen flowing in circular channels of various diameters ranging from 3 μm to 82 μm. For both the laminar and the turbulent regimes, friction factors were slightly smaller than predicted by the Moody chart. Heat transfer coefficients in the turbulent regime were significantly higher than for large channels. The flow could not be considered incompressible due to the large pressure gradients in the tubes. A compressible flow analysis, therefore, was used in reducing the data.

Wang and Peng (1994) investigated single-phase forced convection of water and methanol in rectangular microchannels with hydraulic diameters ranging from 0.311 to 0.747 mm for Reynolds numbers less than 4×10^3. By observing augmented heat transfer coefficients, they found that the transition to turbulent flow was initiated at Reynolds numbers of 1000-1500. They also reported that their heat transfer data for this Reynolds

number range (i.e, 1 x 10^3 to 4 x 10^3) could be well predicted by a modification of the Dittus-Boelter equation in which the constant has been changed from 0.023 to 0.00805. Liquid temperature, velocity and microchannel size all strongly affected the heat transfer behavior.

Recognizing the apparent lack of systematic research on heat and momentum transport in microchannels, Yu *et al.* (1995) studied the fluid flow and heat transfer characteristics of dry nitrogen gas and water in circular tubes with diameters of 19 μm, 52 μm and 102 μm. Both laminar and turbulent regimes were studied with Reynolds numbers ranging from 250 to nearly 2 x 10^4 and Prandtl numbers of 0.7-5.0. Friction factors were slightly lower than the Moody chart values for both laminar and turbulent regimes. Nusselt numbers for the cooling of water in the turbulent regime, however, were considerably higher than would be predicted for larger tubes. This suggests, as does the earlier work of Choi *et al.*, that the Reynolds analogy may not apply for microchannel flow. The heat transfer experiments were performed for the 102 μm tube and with water only.

Adams (1999) investigated the convection heat transfer coefficient in the single-phase, turbulent flow of water in microchannels. Experiments were performed with wall boundary conditions of constant temperature and constant heat flux. The constant wall temperature experiment utilized circular microchannels having inner diameters of 0.76 mm and 1.09 mm. The constant heat flux experiments utilized a circular microchannel and also a microchannel whose cross section geometry was designed to simulate the interior subchannels of the proposed Accelerator Production of Tritium (APT) target bundles. The circular microchannel had an inner diameter of 0.76 mm whereas the

"prototypical" microchannel had a hydraulic diameter of 1.13 mm. Constant heat flux experiments were carried out using both totally degassed water and also water saturated with air at test section inlet conditions for the circular microchannel.

For both microchannels investigated with the constant wall temperature facility, heat transfer coefficients above the values predicted by the Gnielinski correlation were observed. The data clearly showed that the effect of small diameter on single-phase turbulent forced convection is to enhance heat transfer. The heat transfer values increased with decreasing diameter and increasing Reynolds number. Based on his data Adams developed the following correlation to predict the Nusselt number for turbulent heat transfer in microchannels:

$$Nu = Nu_{Gn} \cdot (1 + F) \tag{2.1}$$

Where

$$F = C \cdot \mathrm{Re} \cdot \left(1 - \left(\frac{D}{D_o} \right)^2 \right) \tag{2.2}$$

And Nu_{Gn} is the Nusselt number as calculated by the Gnielinski correlation. A least squares fit of the entire data set resulted in $C = 67.6 \times 10^{-5}$ and $D_o = 1.164 \times 10^{-3}$ m. The correlation is valid for the following parameter range:

$$2 \times 10^3 \leq Re \leq 2.3 \times 10^4$$

$$1.54 \leq Pr \leq 6.43$$

$$0.102 \text{ mm} \leq D \leq 1.109 \text{ mm}$$

With a 95% confidence level, all the data are predicted by the correlation within ±18.6%. With the correlation cast in this form, D_o represents diameter above which no heat transfer enhancement is observed and traditional correlations are valid.

Adams, et al. (1999) examined heat transfer enhancement due to the desorption of noncondensable gases in microchannel flow; they reported that such enhancement occurs at relatively low void fractions, the enhancement increasing with increasing void fraction. More enhancement is observed at the same void fraction for lower turbulent Reynolds numbers. These trends are consistent with the two-phase, two-component heat transfer literature. The most well suited available correlation for predicting heat transfer enhancement, however, greatly under-predicts the experimentally observed heat transfer enhancement due to desorption. Results from the noncondensable gas desorption model showed that significant voidage can occur in the turbulent microchannel flow of water saturated with a noncondensable gas at inlet conditions; in some cases, choking can occur. Desorption in turbulent microchannel flow is a complicated phenomenon affected by microchannel diameter, length, flow rate, heat flux, subcooling and noncondensable species.

In the literature cited, there is a notable degree of disagreement as to the effect of small flow passages on both momentum and heat transfer. In addition, the majority of the research cited was conducted using rectangular flow passages while ignoring the effect of aspect ratio. Of further interest is the fact that although flow gaps (ie.e the height of the flow passages) were often as small as a fraction of a millimeter, the widths of the flow passages were often much larger. In some cases where the width of the flow passages were comparable to the flow gaps, hydraulic diameters larger than the 2 mm

limit resulted for which Kakac, Shah, and Aung expressed their reservations. With the exception of Yu, *et al*., it seems as though no research is available which pertains directly to the effect of small diameter on the turbulent forced convection of water in circular tubes. More importantly, no reliable experimental evidence has been found as to the smallest size channel for which traditional Nusselt number correlations can be applied without significant error.

CHAPTER III

INSTRUMENTATION AND EQUIPMENT

The Georgia Tech Microchannel Test Facility (GTMTF) was used for the entirety of this investigation. The GTMTF is a general purpose test facility designed for investigating flow phenomena in microchannels. The GTMTF was originally used by Kennedy, et al. (1997) and Roach (1998) to study OFI and CHF in microchannels with circular cross sections and with cross sections designed to replicate coolant channels in micro-rod bundles. Blasick (1999) and Stoddard (2000) later modified the facility to study OFI and CHF in test sections with annular flow passages simulating the innermost coolant channels APT targets. This chapter details the modifications and final configuration of the GTMTF used for OFI and heat transfer coefficient experiments for thin, rectangular test sections.

3.1 Georgia Tech Microchannel Test Facility Overview

The GTMTF design criteria, as clarified by Stoddard (2000), Kennedy, et al.(1997), Roach (1998), and Blasick (1999), were as follows.

1) To provide a stable, controllable, and measurable flow of water through the test section over a broad range of mass fluxes.

2) To provide for a flexible system configuration and the possibility of running experiments with and without a test section bypass line.

3) To allow for control and measurement of the dissolved non-condensable gas content within the system.

4) To allow for fine control and measurement of the test section inlet temperature

5) To allow for fine control and measurement of the test section exit pressure.

6) To provide stable, controllable, and measurable electrical power for heating of the test section.

The details of the GTMTF hardware and instrumentation are outlined in the remaining sections of this chapter. The range and accuracy of the instruments are discussed, along with their incorporation into the data collection method. Furthermore, three major categories are covered in the discussion of the experiment's hardware configuration.

1) The design and mounting of the test section, along with its peripheral hardware
2) An updated list log of hardware in the GTMTF, including manufacturer information and location.

Figure 5.□ The saturation loop used to ensure fully nitrogen-saturated coolant.

3.2 Test Section Design and Mounting

The goal of this investigation was to develop OFI correlations and heat transfer data for a narrow rectangular cross-section. Therefore the first step was to configure a test section that had a rectangular cross-section along with the ability to be heated uniformly. To achieve these design specification a .375" 302 SS tube with .01" thickness was used. The middle 12 inches of the two foot long tube were compressed into a rectangular geometry, approximately .070" by .561". Figure 3.1 shows the design specifications of the final compressed tube used in the investigation.

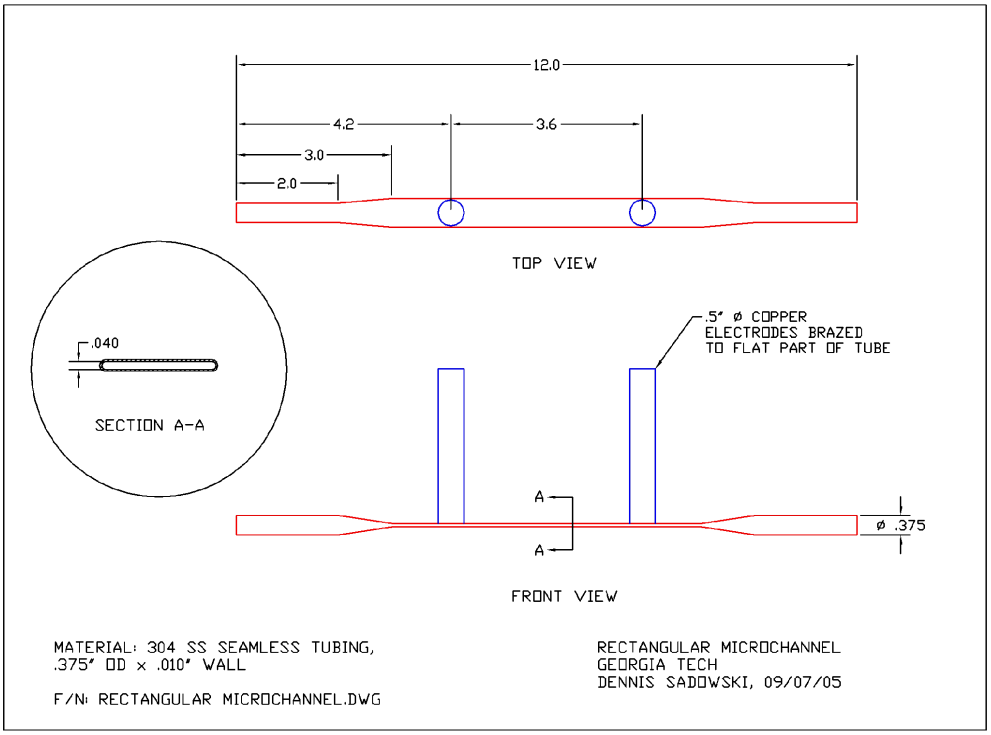

Figure 3.1: Design Specifications of the Microchannel Test-Section

In order to connect the test section to the GTMTF, Swagelok fittings were attached to the tube ends. PVC T-fittings were used on both ends of the test section to ensure electrical isolation from the rest of the GTMTF.

3.2.1 Test Section Insulation

To prevent excessive heat loss the test section was insulated with two layers over the entire heated length. The first layer was comprised of two Marinite blocks on either side of the heated segment of the test section. As shown in Figure 3.3, the Marinite blocks had 6 holes drilled through them in order to fit six quarter inch copper screws. Marinite had two properties that were desired, a high temperature threshold and a high electrical resistance. This ensured that if an accidental burnout occurred there would be no permanent damage to the insulation. It also guaranteed that there would be no

alternative paths for the electrical current going through the test section to travel through. The Marinite screw holding strength is only 91.0 kg, therefore a stronger material was used as a backing to the Marinite for the screws. Garolite, a layered glass fiber material bonded by epoxy, was chosen for this backing because of its high strength and insulation properties. Unfortunately Garolite has a low threshold for temperature, only 180ºC, therefore the dual layer design of the insulation was required to take advantage of each material's strength. Further insulation was deemed unnecessary, because wall temperature readings both before and after the heated length showed there was negligible heat loss past the copper nodes. Figure 3.2 shows the design of both the inner and outer insulation layers.

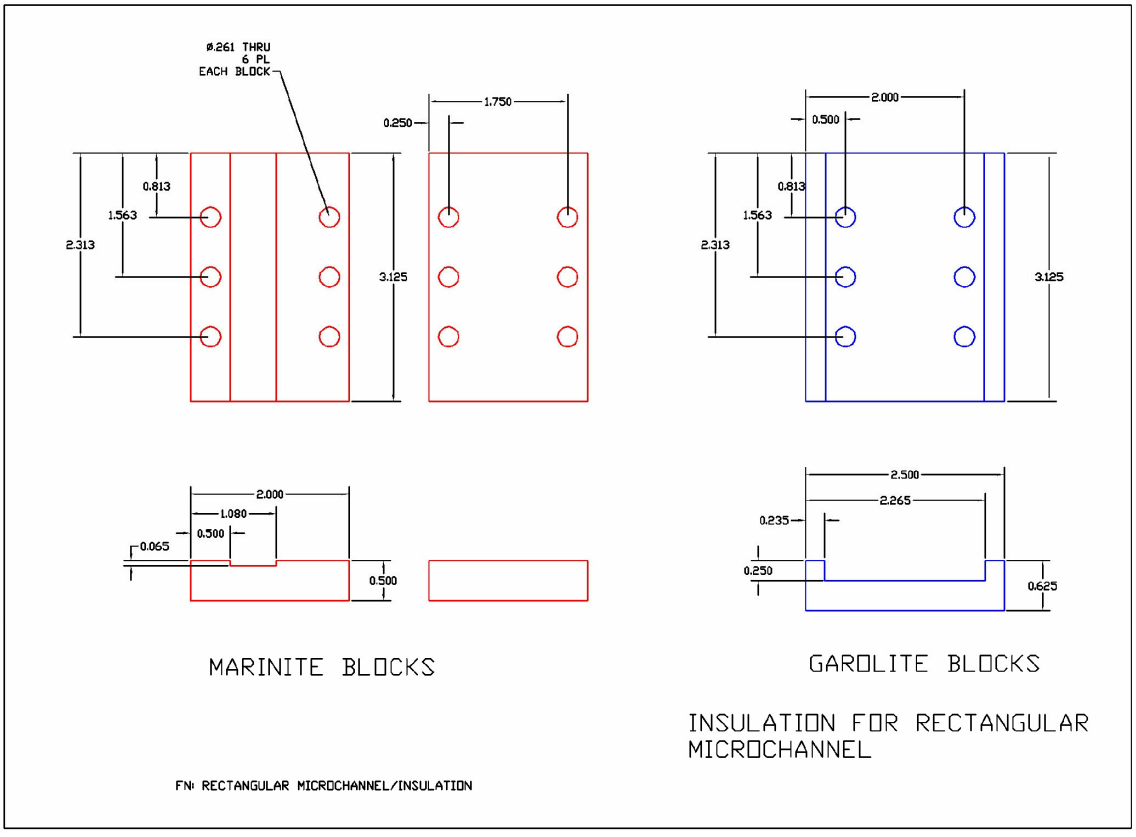

Figure 3.2: Design Specification of Garolite and Marinite Blocks

3.2.2 Test Section Mounting

The test section used in this investigation was mounted vertically, with the insulation and copper blocks adding a significant amount of weight. The supports had to accommodate this weight, without pinching the thin walled test section or providing a path for the electrical current. Unistruct was used as the basis of the mounting configuration, with two vertical segments being bolted to the GTMTF.

The right-hand side Unistruct supported the large copper cables, preventing any potentially damaging torque forces from acting on the test section. These cables were fixed to the Unistruct via the Power Cable Mounting Block (PCMB), diagramed in Figure 3.4.

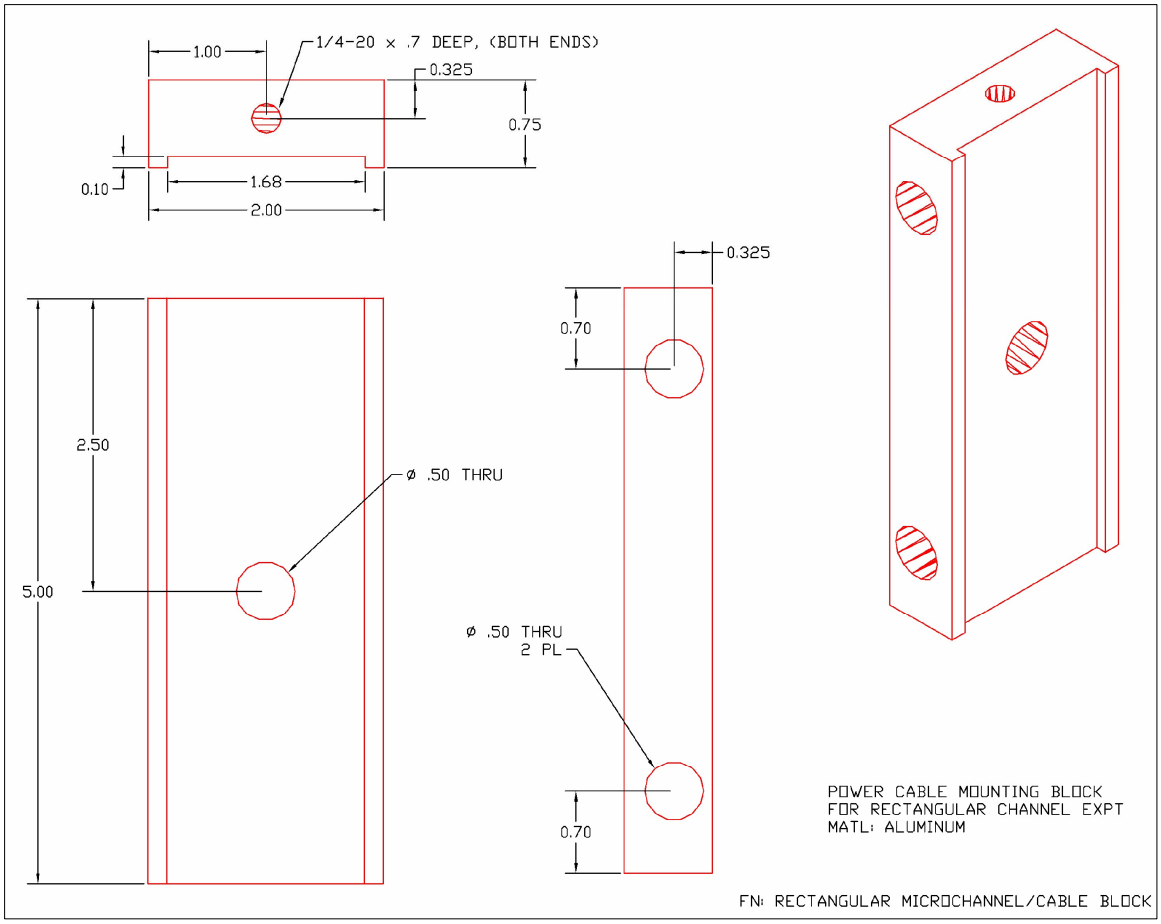

Figure 3.3: Design Specifications of the Power Cable Support Block

The PCMB was bolted to the Unistruct using a ½" Bolt through the center hole. Circular Aluminum hoops were secured around the two 1000 MCM copper cables and then attached to rods that were fed through the two 0.325" holes in the Cable Block. These rods carried the entire weight of the copper cables, thereby eliminating any excessive moments from acting on the test section. It should be noted that the Aluminum hoops were attached over the cable's insulation, complying with the goal of keeping the test section electrically isolated.

The left-hand side Unistruct was used for the mounting of the Garolite Support Block. Garolite was chosen as the support material because of its electrical resistance. Two Garolite blocks connected to the Garolite Support Block and extended to the test section. These blocks had half circles fitted to the test section cut out at their ends. Two more small Garolite blocks with the same half circle cut out were bolted to the first blocks, thereby securing the test section. These blocks were fitted to the annular parts of the test section, rather than the more fragile rectangular portion.

After being mounted and attached to the power supply loop the test section was connected to the fluid flow loop. This connection had to be electrically insulated and strong enough to hold up to 100 psia. For this reason PVC Tee's were used. However, PVC does not have good thermal strength, so the exit PVC Tee was placed downstream of a foot long SS tube which allowed the coolant temperature to decrease before reaching the PVC Tee fitting.

3.3 Power Supply configuration

The test sections in this investigation were all used to heat the bulk fluid flowing through them. Therefore, a continuous current had to be supplied and maintained to the test section. The following subsections describe the power supply used to provide this current, along with details of the power measurement system.

3.3.1 Power unit

As shown in Figure 3.3, the power supply configuration used a DC/AC power supply produced by Rapid Power Technologies (serial number: 1198224) to supply electrical power to the connected heater. The power level produced by this DC power supply was controlled using a set of two rheostats. The first rheostat controlled the maximum current produced by the power supply (in percentage), with 100% representing a potential maximum current of 2500 Amps. The second rheostat controlled the voltage drop produced by the power supply (in percentage), with 100% representing a maximum electrical potential of 25 Volts. These two rheostats, placed internally, are not shown in Figure 3.3.

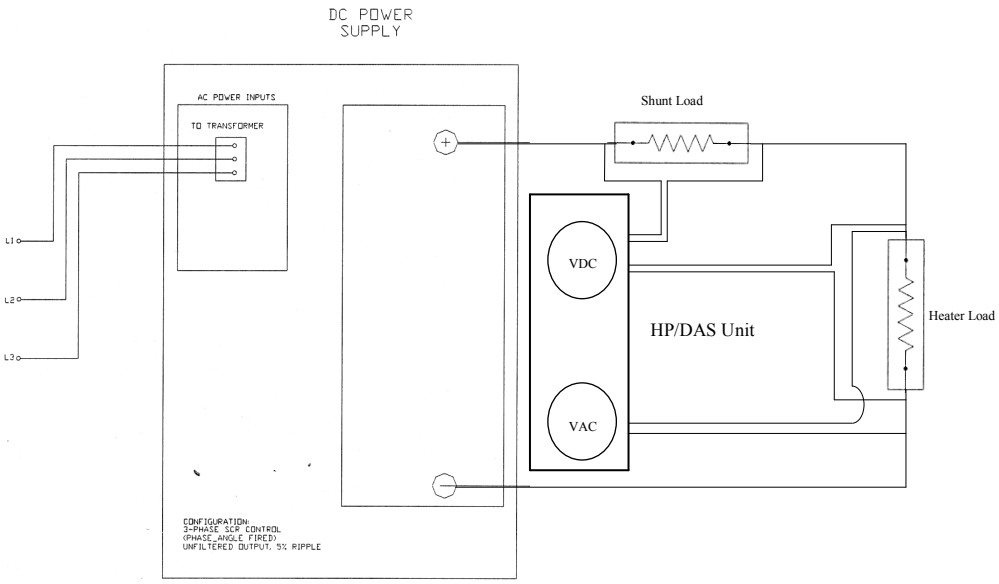

Figure 3.4: Power Loop Schematic

3.3.2 Power Loop Configuration

The power supply loop began at the positive node of the DC power supply and ran through an Empro DC current shunt and on to a flexible, 1000 MCM, copper cable. Next, power was applied directly to the test section using a copper electrode block. The 1000 MCM copper cable bolted directly to this electrode plate using a single ½"-13 bolt; the hole for this bolt was drilled in the center of the block. After passing through the test section, the supply loop was completed by a second copper electrode block that was connected to the negative node of the DC power supply via a second 1000 MCM copper cable.

3.3.3 Power measurement

The experimental setup measured the power output using the HP/DAS system. The power supplied by the Rapid Power Transformer is unique in that it has both a DC and AC component. Therefore an effective power had to be calculated that incorporated

both the DC and AC components. This effective power was calculated using the following equation.

$$P_e = V_e A_e \qquad \text{(EQ 3.1)}$$

Where;

V_e = Effective Voltage

A_e = Effective Current

Two voltage reading leads from the HP/DAS system were connected to each of the copper electrode blocks mounted on the test section. The effective voltage was calculated from the DC voltage and the AC voltage using the following equation.

$$V_e = \sqrt{\left(V_{DC}^2 + V_{AC}^2\right)} \qquad \text{(EQ 3.2)}$$

Similarly, two leads from the HP/DAS system were connected to each end of the Empro Shunt in order to calculate the current. However, during experimentation it was discovered that the AC voltage reading was experiencing a large pickup from the background noise being generated by the large Rapid Power Technologies unit. Therefore, a backwards calculation was developed on the assumption that the DC to AC power ratio was constant throughout the power supply loop. This backwards calculation is shown below.

$$V_{AC\_S} = \frac{V_{AC\_TS} \cdot V_{DC\_S}}{V_{DC\_TS}} \qquad \text{(EQ 3.3)}$$

The resulting AC voltage drop was combined with the DC voltage drop and then combined using Equation 3.2, finally being converted to a current using the shunt multiplier.

$$A_e = M\sqrt{\left(\left(V_{AC\_S}\right)^2 + \left(V_{DC\_S}\right)^2\right)} \qquad \text{(EQ 3.4)}$$

Where;

M = Shunt Current-to-Voltage Multiplier

3.4 Flow Loop Configuration

The flow loop's arrangement must first be defined before detailing the subcomponents. Figure 3.5 shows a schematic diagram of the GTMTF components and instrumentation used in the flow loop configuration. The labels employed within the diagram are cataloged and described in Tables 3.1 and 3.2. This flow loop configuration was used for all experiments performed during the investigation.

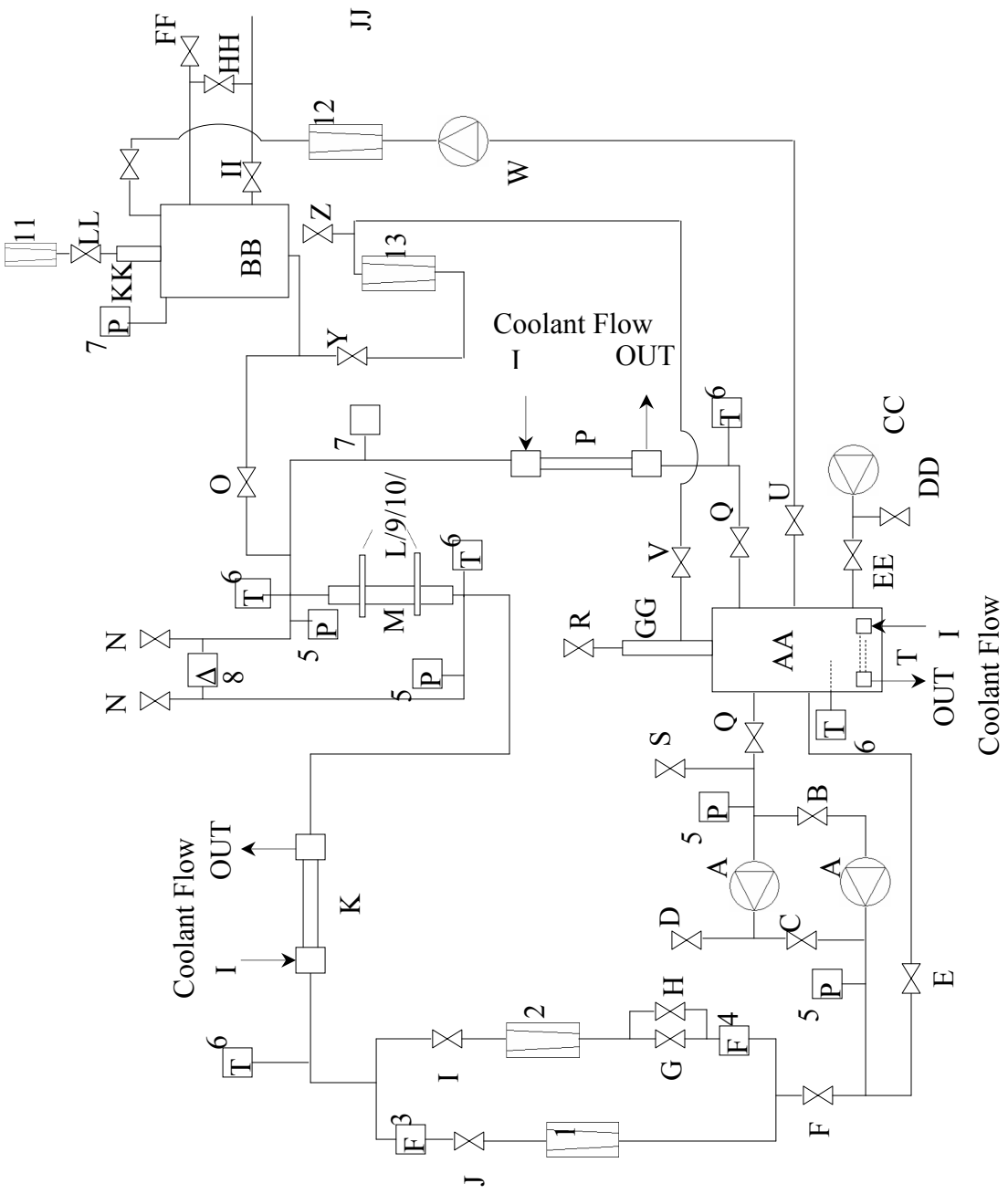

Figure 3.5: Schematic Diagram of the Georgia Tech Microchannel Test Facility

Table 3.1: Listing of GTMTF Hardware Components

Label	Description	Manufacturer	Model
A	Multi-stage centrifugal pump	Teel	2PC45
B	Pump isolation valve 1	-	-
C	Pump isolation valve 2	Watts	CF8M
D	Lower drain valve	-	-
E	Pump bypass valve	Whitey	SS-12NBS8-SH
F	System throttling valve	Watts	CF8M
G	High flow metering valve (coarse)	Whitey	SS-3NBF4
H	High flow metering valve (fine)	Parker	4Z(A)-V2LR-SS
I	High flow/Test section isolation valve	Watts	CF8M
J	Low flow metering valve	Nupro	SS-4LA
K	Test section heat exchanger (tube-in-tube)	Parker Hannifin	DHTC-SS-8
L	Copper node	In house constr.	-
M	Test section	-	-
N	Bleed valves	Hoke	1513G4S
O	Saturation tank pressure regulation valve	Whitey	SS-3NBF4
P	System heat exchanger (tube-in-tube)	Parker Hannifin	DHTC-CU-6
Q	Degassing tank isolation valve	Teel	A743-CF8M
R	Degassing tank bleed valve	Whitey	SS-IRS8
S	System drain valve	Watts	CF8M
T	Degassing tank heat exchanger	In house construction	
U	Degassing tank outlet isolation valve	Whitey	SS-3NBF4
V	Degassing tank inlet isolation valve	Whitey	IRS4
W	Saturation/degassing tank recirculation pump (magnetically coupled gear)	Micropump	185
X	Saturation tank inlet isolation valve	Parker	3C6C-202B
Y	Saturation tank outlet isolation valve	Whitey	SS-3NBF4
Z	Bleed Valve	Parker	-
AA	Degasing tank	In house construction	-
BB	Saturation tank	In house construction	-
CC	Variable-speed positive displacement pump (□eparation□)	Masterflex	7018-20
DD	System pressure relief valve	Parker	2030 CBBI-1
EE	System Water fill valve	Jones Mfg. Co.	150 WSP
FF	Saturation tank blow-off valve	Parker	2030 CBBI-1
GG	Degasing tank gas □eparation column	In house contruction	-
HH	Saturation tank bubbler select valve	Hoke	1513 G4S
II	Saturation tank gasfill valve	Parker	2030 CBBI-1
JJ	saturation tank compressed Nitrogen supply cylinder	-	-
KK	Saturation tank liquid seperatio column	In house construction	-
LL	Saturation tank gas bleed valve (integrated with flowmeter)	Omega	5-65 C

Table 3.2: Listing of GTMTF Instrumentation

Label	Description	Manufacturer	Model	Serial Number
1	Rotameter, low range	Fischer & Porter	10A6132N	8712A0041A1
2	Rotameter, high range	Brooks Instruments	1305D08A1A1A	8603HC013
3	Liquid Flow Transducer	EG&G/FTI	FT0-3/RI-51	F096107517RI189010
4	Liquid Flow Transducer	EG&G/FTI	FT0-8/RI-51	804950RI5189030042
5	Pressure Transducer	Rosemount	1144A-0200A22	Multiple
6	Thermocouple,Type-E	Omega	EMQSS-125G-6	None
7	Pressure Gauge, Bourdon tube type	Various	Multiple	Multiple
8	Differential Pressure Transducer	Rosemount	1151DP5E22	1072957
9	AC-lead (test section) to HP unit	-	-	-
10	DC-lead (test section) to HP unit	-	-	-
11	Rotameter	Omega	5-65C	none
12	Rotameter	Fischer & Porter	10A6131M	8911A0675A17
13	Rotameter	Fischer & Porter	10A6131M	8911A0675A17
14	DC-lead (shunt) to HP unit	-	-	-
15	Data Acquisition / Switch Unit	Hewlett Packard	HP 34970A	GT 0091257

Table 3.2 (continued)

Label	Manufacturer Stated Range	Manufacturer Stated Accuracy	Calibration Source	Calibration Date
1	1.5 ─ 21 gph, water	0.5 gph	-	-
2	0.2 ─ 2.5 gpm, water	0.1 gpm	-	-
3	0.02 ─ 0.4 gpm	0.1% repeatability	Becht, GT	-
4	0.2 ─ 10 gpm	0.1% repeatability	Becht, GT	-
5	1 ─ 1375 kPa	0.25% cal.range	Becht, GT	-
6	-200º ─ 425ºC	0.1ºC	Becht, T	-
7	0 ─ 200 psi	2 psi	-	-
8	0 ─ 750 inch H_2O	0.2% calibrated range	Becht, GT	-
9	-	-	-	-
10	-	-	-	-
11	0 ─ 9 gph,water	1 gph	-	-
12	0 ─ 3.4 scfm, air	0.2 scfm, air	-	-
13	0 ─ 3.4 scfm, air	0.2 scfm, air	-	-
14	-	-	-	-
15	100 Mv ─ 300v -150º ─ 1000ºc	0.0040% of reading	Manufacturer	-

3.3.1 System Instrumentation

Table 3.2 provides a list of measuring instruments used in the GTMTF along with their manufacturer, model number, range, and accuracy.

3.3.1.1 Absolute Pressure Transducers

Four Rosemount model 1144A transducers (Components 5 of Figure 3.4) were utilized in the GTMTF to measure test section inlet and exit pressures and pump inlet and exit pressures. All four transducers were mounted at the bottom of the GTMTF in order to avoid entraining air bubbles in the transducer.

3.3.1.2 Differential Pressure Transducer

In order to measure the differential pressure across the test section, one differential pressure transducer (Component 8) was mounted on the GTMTF. The transducer used was a Rosemount style 1151DP, with a differential pressure range of 0 – 750 inch H_20. The pressure transducer was mounted above the test section which caused entrained gas bubbles to become trapped in the transducer. To avoid any reading errors two bleed valves (Components N) were installed above the pressure transducer in order to rid the differential pressure transducer of any trapped air pockets.

3.3.1.3 Turbine Flowmeters

Two EG&G turbine flowmeters (Components 3 and 4) were used to measure the flowrate through the test section. The flowmeters were installed upstream of the test section in a horizontal orientation to ensure accurate readings and calibration.

3.3.1.4 Rotameters

Two rotameters (Components 1 and 2) were mounted in the GTMTF to allow a visual reference of the flowrate through the primary flow loop. Two additional rotameters (Components 12 and 13) were mounted in the saturation flow loop to monitor and control the flow into and out of the saturation tank. The rotameters had flow control valves on them allowing the flow to and from the saturation tank to be balanced. This flow balance was required to prevent flooding or drying of the saturation tank, while still serving the purpose of saturating the coolant. All four rotameters provided general readings to assist with control of the GTMTF; none of them provided information essential to the experimental data.

3.3.1.5 Thermocouples

All thermocouples (Components 6) used in the GTMTF were Omega type-E with stainless steal sheaths. Swagelok compression fittings were used to ensure the tips of the thermocouples were positioned near the center of the water stream. Additionally, three type-E thermocouples were placed on the wall of the heated portion of the test section. These three thermocouples were used to measure the wall temperature necessary to calculate the heat transfer coefficient for both turbulent and laminar regimes.

3.3.1.6 Pressure Gauges

Two pressure gauges (Components 7) were used to provide a visual reference of the pressure levels in the system; these gauges, like the rotameters, were not used to

provide information essential to the experimental data. The test section exit pressure was measured using a McDaniel Controls, Inc. pressure gauge rated for 0 – 200 psig. This gauge was used during the system filling procedure in order to prevent over pressurization. It was necessary to prevent the system pressure exceeding 20 psig because the peristaltic pump (Component CC) was not rated for high pressure operation. The saturation tank pressure was monitored using a Span Instrumentation pressure gauge, rated for 0 – 300 psig.

3.3.1.7 Hewlett Packard Data Acquisition / Switch Unit

The Hewlett Packard Data Acquisition / Switch unit was used during all experiments to collect and compile the data from the GTMTF instrumentation. HP Benchlink Data Logger Software operating on a Microsoft Windows 95 interface was used as the interface to store and operate on the data collected by the HP unit.

CHAPTER IV

EXPERIMENTAL PROCEDURES

The focus of this chapter is to provide a complete and accurate record of the system preparation and control procedures. A majority of the preparation procedures were derived from previous experiments performed on the same experimental setup; Kennedy, et al. (1997), Roach (1998), Blasick (1999), and Stoddard (2000).

4.1 Power Preparation

The first step in preparing the system was ensuring a fully conductive connection between the power supply and the test section. First, the copper nodes were cleaned using plumbers wire, preparing the surface for silver paste application. The copper nodes were then secured to the test section after a small amount of silver paste was dabbed on the test section. Any silver paste extending beyond the nodes had to be wiped away to prevent alternate paths for the electricity. It was only necessary to perform this procedure when the test section was not used for extended periods of time.

4.2 System Filling Procedure

The goal of the system filling procedure was to eliminate all air pockets formed by the first bulk filling. This was accomplished by a repetitive process explained in the following section.

The saturation tank gas bleed valve (component LL in Figure 4.1) was always left open to the atmosphere to allow Nitrogen gas to bubble through the saturation tank (Component BB). The saturation loop therefore had to be isolated during the initial filling of the GTMTF, because the filling procedure required slight pressurization. Any

attempt to pressurize the system would have resulted in an overflow out of the bleed valve. In order to isolate the saturation loop the degassing tank outlet valve (Component U), the degassing tank inlet valve (Component V), and the saturation tank regulation valve (Component O) were all closed. After the saturation loop was isolated, the system was filled with distilled water using a variable speed peristaltic pump (Component CC). Prior to filling the GTMTF with the peristaltic pump, the system relief valve (Component DD) was opened and the peristaltic pumped turned on, to allow any trapped air to escape from the peristaltic pump tubing. When the flow out of the system relief valve was free of trapped air the valve was closed and the system fill valve (Component EE) was opened, allowing water to flow into the degassing tank (Component AA). Once distilled water was flowing into the GTMTF, the system drain valve (Component S) was opened. The system drain valve (Component S) was closed and the degassing tank bleed valve (Component R) was opened, once water began flowing out of the system drain valve. When water began running out of the degassing tank bleed valve the two bleed valves (Components N) above the differential pressure transducer (Component 8) were opened. When water flowing out of the bleed valves was free of air bubbles all three valves were closed.

The system was pressurized to 20 psig once all the valves were closed. After pressurization, the peristaltic pump was turned off and the system fill valve (Component EE) was closed. Next the system throttling valve (Component F) was fully shut, and the pump bypass valve (Component E) was opened. This was done to prevent any damage to the liquid flow transducers by a fluid thrust during startup of the pumps. All remaining internal flow valves were opened to allow complete flow throughout the GTMTF. After

the valves were properly set, one of the two Centrifugal pumps (Components A) was turned on. The system throttling valve was then slowly opened, allowing flow throughout the loop.

After five minutes of operation the pump was turned off. The same three valves that were previously closed, the differential pressure transducer bleed valves (Components N), and the degassing tank bleed valve (Component R) were all opened. This allowed air pockets that accumulated during operation of the pump to escape the system. The System fill valve (Component EE) was then opened and the peristaltic pump (Component CC) was turned on. The three bleed valves were toggled during operation of the peristaltic pump in order to flush out any air pockets. After approximately a minute all three bleed valves were closed and the system was pressurized to 20 psig. Following the previous procedures, the peristaltic pump was shut off and the system fill valve closed after pressurization. Next, the system throttling valve (Component F) was closed and the centrifugal pump (Component A) that wasn't used previously was turned on.

The process of running the pumps, bleeding off the air pockets, and refilling the flow loop was repeated until no air could be seen in either the flow through the rotameters (Components 1 and 2) or escaping the bleed valves. Once the system was completely free of trapped air, it was pressured to 20 psig.

The filling of the saturation loop could proceed once the system was free of air pockets. First, the Saturation inlet valve (Component U) was opened to allow water to flow from the degassing tank into the saturation loop. No additional air passed into the primary flow loop because the system was pressurized to 20 psig and the saturation tank was open to the atmosphere. Next, the peristaltic pump (Component CC) was turned on

and the system fill valve (Component EE) was opened. Once water began flowing in through the system fill valve, the saturation loop exit valve (Component V) and the saturation tank pressure regulation valve (Component O) were opened. The saturation loop bleed valve (Component Z) was closed once water began flowing out of it. Both the bleed valve (Component Z) and the Saturation/degassing tank recirculation pump (Component W) were toggled in order to release any air in the saturation inlet line. When no air could be seen escaping the saturation loop bleed valve it was shut. Filling continued until water began flowing out of the Saturation tank blow-off valve (Component FF), at which point the peristaltic pump was turn off, and the system fill and blow-off valves were shut.

4.3 Working Fluid Nitrogen Saturation and System Pressurization

Prior to the start of any set of OFI or heat transfer coefficient experiments, the system fill procedure, as outlined in Section IV.2, was followed. After completion of the fill procedure the system had to be pressurized to a specific level and the water saturated with nitrogen.

First, to achieve the saturation and pressurization of the working fluid, the saturation tank recirculation pump (Component W) was started. This pump drew water from the degassing tank (Component AA) into the saturation tank (Component BB). Next the Compressed Nitrogen supply cylinder (Component JJ) was opened and its regulator set to the desired experimental pressure. The saturation tank gas fill valve (Component II) was then slowly opened, allowing the nitrogen gas to bubble up through the saturation tank (Component BB). Care was taken to avoid rapid pressurization of the system. Once the pressure between the saturation tank and the supply cylinder was

equalized, the saturation tank gas bleed valve (Component LL) was slightly opened. This ensured that Nitrogen gas would bubble through the saturation tank and keep the working fluid fully saturated. Two rotameters (Components 12 and 13) were used to adjust the saturation tank inlet and outlet flowrates; balancing them in order to prevent dryout or flooding of the system. Once the flowrates were balanced and the nitrogen gas was bubbling out of the saturation tank gas bleed valve, the system was ready for operation.

4.4 Test Section Inlet Temperature Control

The two primary systems used to cool the flow during OFI experimentation were the system heat exchanger (Component P) and the degassing tank heat exchanger (Component T). However, the most precise method of control for the test section inlet was the test section heat exchanger (Component K). This heat exchanger was connected to a constant temperature bath which allowed for precise control of the cooling fluid temperature, though the coolant flowrate could not be controlled. As the working fluid's flowrate changed during operation, so did the heat transfer coefficient of the heat exchangers. For this reason the temperature of the bath typically had to be adjusted at several key points during operation to maintain a steady state inlet temperature. While the other two heat exchanger's flowrates could be changed, their coolant was the house water line (17ºC – 20ºC), preventing any control of heat exchanger temperature. For all of the OFI experiments the maximum possible flowrate was used for the system heat exchanger and the degassing tank heat exchanger. Only the test section heat exchanger parameters were varied to regulate the test section inlet temperature.

4.5 OFI Experimental Procedure and Analysis Techniques

4.5.1 OFI Experimental Procedure

Once the system was running and all the experimental control variables were set, an OFI experiment could be performed. To prevent burnout each OFI experiment always started with a very high flow rate with the power supply unit shut off. The power supply unit was then turned on and slowly raised to the desired output level. In order to reach steady state conditions the system was allowed to run for a few minutes. As explained in Chapter III, the HP DAS system acquired data from the GTMTF once every seven seconds and recorded the data using the Benchlink Data Logger Software on a Microsoft Windows 95 operating system.

With all system control variables set properly, all systems functioning correctly, and data being acquired every seven seconds by the HP DAS system, the mass flux through the test section was decreased by increments of approximately 0.25 to 1 gal/hr every seven to fourteen seconds until the test section differential pressure reached a minimum and began increasing. This increase in differential pressure indicated that the flow had passed through OFI and was operating in the negatively-sloped region of the demand curve. In order to ensure accurate readings at the OFI point, the incremental decrease in flow rate was smallest as the flow conditions approached OFI. Once OFI was surpassed, the experiment was terminated by first shutting off the power supply unit. The pumps were not immediately shut off to allow for continued cooling of the test section post experiment.

4.5.2 OFI Experimental Analysis Techniques

Once the experiment was terminated, the data was compiled and a demand curve for the experiment was generated. The demand curve directly provided the OFI conditions, with OFI defined for most experiments as the flow rate at which the test section differential pressure reached a minimum. For certain experiments this point was not clear and therefore a 3rd order polynomial fit was applied to the pressure drop data near the OFI region to estimate the flow rate at which the differential pressure reached a minimum. Figure 4.1 shows a typical experimental demand curve where the OFI point is the point with the minimum differential pressure. A plot similar to Figure 4.1 was generated for every OFI experiment conducted. The data from each of these experiments is compiled and listed in Appendix B.

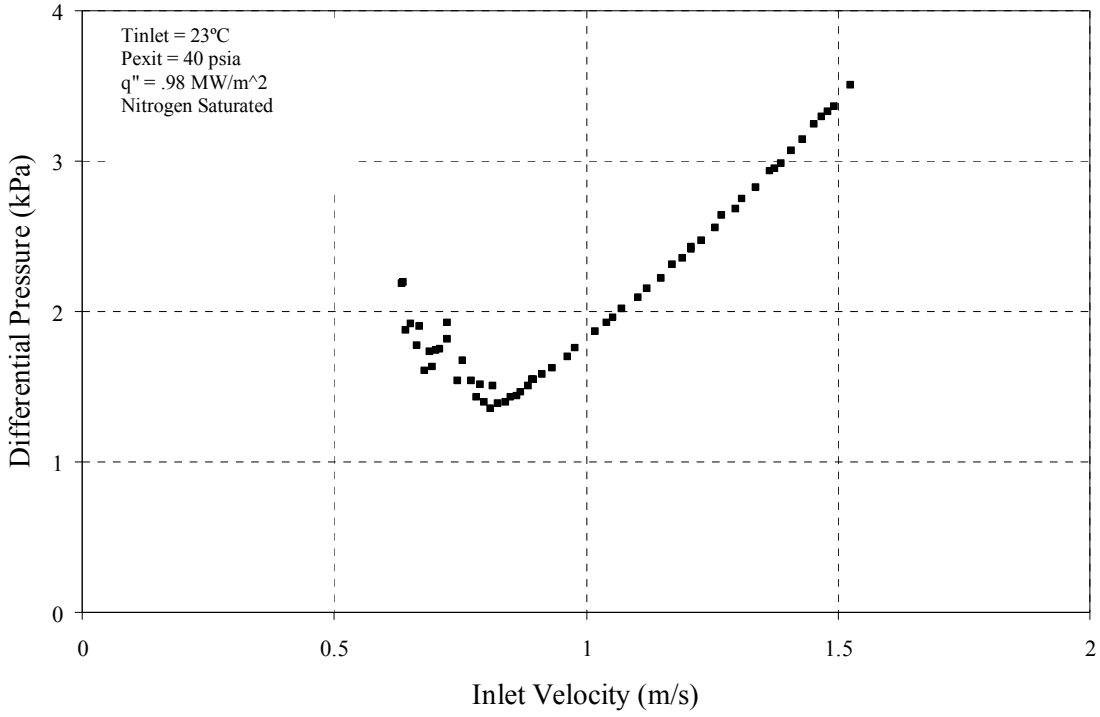

Figure 4.1: Typical Experimental OFI Demand Curve

As discussed previously several experimental parameters were recorded by the HP DAS system described in Section III.3.1.7. These parameters included test section inlet and outlet pressures, test section inlet and outlet temperatures, volumetric flow rate, and total power output from the power supply. Using these parameters, inlet and exit water conditions could be determined and used to perform an energy balance on the test section. It was possible to quantify the heat loss to the environment using this energy balance because the power input to the test section was maintained at a prescribed value. The heat loss to the environment was required to determine the exact surface heat flux at OFI. The following paragraphs outline the energy balance procedure used in analyzing all OFI data.

First, using the inlet and exit temperatures and pressures, the inlet and exit enthalpies were determined using the Engineering Equation Solver (EES) algorithm shown in Appendix A. The nature of OFI experimentation dictated that each experiment began with single-phase liquid water flowing through the test section and ended with single-phase liquid water transitioning to a two-phase liquid-vapor mixture within the test section. Furthermore, the exact quality of the two-phase liquid-vapor mixture exiting the test section was unable to be determined due to lack of proper instrumentation. As such, the exit enthalpy and density found using EES was only valid while single-phase liquid water was exiting the test section. This limitation required using the following techniques to determine the exact surface heat flux at OFI.

As stated earlier, the power input to the test section was set and maintained at a prescribed level for each OFI experiment. This power level was recorded every seven seconds using the voltage drop meters on the test section, along with the voltage drop meters at the shunt. As stated earlier, the HP DAS system recorded the total power supply output in addition to the water conditions at the inlet and exit of the test section. While the coolant was single-phase, an energy balance performed on the coolant using inlet and exit enthalpy and mass flow rate could be compared to the recorded total power supply output in order to determine the power lost to the environment. This loss was then averaged over the last ten single-phase ($x = 0$) data points and applied to the two-phase regime of the experiment. This provided the actual power absorbed in the working fluid at OFI. The average surface heat flux was then calculated by simply dividing the total power absorbed in the working fluid by the total heated surface area. The assumption of constant external heat loss was deemed to be appropriate because the test section and

fluid temperature stay nearly constant in the flow-boiling regime. The losses generally accounted for 8 percent of the total power supply output. It's important to note that total power supply output refers to the calculated power influx to the test section using the voltage drop across the two copper nodes. Any power lost to previous power loop components, such as the shunt used for current calculations, was not included in the calculations. Heat loss from the power supply configuration was primarily limited to the copper nodes that connected the power supply cords to the test section tubing. These copper nodes acted as heat sinks and drew heat from the test section. Further heat loss can be attributed to conduction within the test section's wall; however due to the limited cross section area of the wall this conduction would have been minor compared to the conduction through the copper nodes.

The energy balance technique just described provided an estimate of the amount of heat lost to the environment from the test section, and, thus, had a significant impact on the "exact" calculated OFI heat flux for the experiment.

The OFI mass flux, average exit pressure, and average inlet temperature for each OFI experiment were found in the following manner. The average inlet temperature was the mean inlet temperature over five data points centered about the OFI point. Likewise, the average exit pressure was the mean exit pressure over the five data points centered about OFI. The standard deviation for the temperature was calculated for each experiment and can be found in Appendix B. The OFI mass flux, $G_{OFI,}$ for each OFI experiment was found by first calculating the mass flux at each data reading taken during the OFI experiment and then picking the value that corresponded to the minimum differential pressure over the duration of the experiment. As described previously, this

value was picked visually or in some cases a third order polynomial fit was used. The mass flux at the data point was found by multiplying the volumetric flow rate through the test section by the inlet fluid density at the liquid flow transducers and then dividing by the flow area of the test section.

The OFI correlations developed in this investigation compare the OFI mass flux to the saturation mass flux and the OFI heat flux to the saturation heat flux. The aforementioned procedures outline the methods used in determining OFI mass flux and OFI heat flux. The following procedures summarize the techniques used in determining the corresponding saturation mass flux and saturation heat flux. They also set forth the methods used in comparing OFI conditions to saturation conditions.

The saturation mass flux refers to the coolant mass flux which would produce saturated liquid at the test section exit for a specified set of flow parameters and power input, i.e., inlet temperature and pressure, exit pressure, flow area, heated area, and average surface heat flux. In order to calculate the saturation mass flux, the inlet enthalpy was determined using the average inlet temperature and pressure at the OFI point. Next the saturation enthalpy of the working fluid (h_f) at the average exit pressure was determined. The difference of the two enthalpy values dictated the required change in enthalpy from inlet to exit necessary to saturate the working fluid. Finally, the saturation mass flux was calculated using the following equation.

$$G_{sat} = q''_{OFI} \frac{A_{heated}}{A_{flow}\left(h_f\left[P_{exit}\right] - h\left[T_{inlet}, P_{inlet}\right]\right)} \qquad (4.1)$$

Equation 4.1 provided the coolant mass flux required to saturate the working fluid at the test section exit given the experimentally fixed value of OFI heat flux at the stated operating conditions (inlet temperature, pressure and exit pressure). Since the OFI mass

flux corresponding to the OFI heat flux used in Equation 4.1 was known, a direct ratio comparison between the OFI mass flux and the calculated saturation mass flux was possible. This provided the means to develop the empirical OFI mass flux correlation to be presented in Chapter V.

Saturation heat flux refers to the average surface heat flux required for the working fluid to become saturated liquid at the test section exit for a given set of flow parameters, i.e., inlet temperature and pressure, exit pressure, flow area, heated area, and coolant mass flux. Once again, the first step in the saturation heat flux calculation was to determine the inlet enthalpy using the average inlet temperature and pressure at the OFI point. Next, the saturation enthalpy of the working fluid at the average exit pressure was found. As previously stated, the difference of these two enthalpy values dictated the required change in enthalpy from inlet to exit necessary to saturate the working fluid. The saturation heat flux was then calculated using the following equation.

$$q''_{sat} = G_{OFI} \frac{A_{flow}\left(h_f\left[P_{exit}\right] - h\left[T_{inlet}, P_{inlet}\right]\right)}{A_{heated}} \qquad (4.2)$$

Equation 4.2 provided the average surface heat flux necessary to saturate the working fluid at the test section exit based on the assumption that the experimentally determined value of OFI mass flux was actually fixed. Once again, since the OFI heat flux corresponding to the OFI mass flux used in Equation 4.2 was known, a direct ratio comparison between the OFI heat flux and the saturation heat flux was possible. This provided the means to develop the empirical OFI heat flux correlation presented in Chapter V.

4.6 Heat Transfer Coefficient Experimental Procedures

Once the flow rate dropped low enough in a heat transfer coefficient experiment to initiate subcooled boiling the experiment was terminated. Key data for calculating the heat transfer coefficient and Reynolds number was then compiled, i.e., inlet temperature and pressure, exit temperature and pressure, volumetric flow rate, wall temperatures, and power input. The following procedures make use of the hydraulic diameter for all the relevant calculations, i.e., Reynolds number, and Nusselt number.

$$D_h = \frac{4 * A_{flow}}{P_{wetted}} \tag{4.3}$$

The flow area and wetted perimeter were calculated using the geometry described in Chapter III.

The first step in determining the heat transfer coefficient was determining the bulk fluid temperatures at the three locations where the wall thermocouples were located. For each location the average power input up to the location had to be calculated.

$$P_x = \frac{X * P_{total}}{L} \tag{4.4}$$

Where X represents the distance from the beginning of the heated length to the location of its corresponding wall thermocouple location, and L represents the total heated length. P_x was calculated for three locations, point 1, point 2, and point 3, and was stored as P_1, P_2, and P_3 respectively. In order to simplify the process, an assumption was made that the pressure inside the test section did not vary significantly from the inlet pressure. This assumption was valid because for sub-cooled liquid, temperature has a much greater effect on enthalpy than pressure. The total power used in Equation 4.4 did not directly

correspond to the power measured by the HP DAS system. Instead the actual power was calculated using an energy balance between the inlet and exit enthalpies.

$$P_{total} = \dot{M}\left(h\left[T_{exit}, P_{exit}\right] - h\left[T_{inlet}, P_{inlet}\right]\right) \tag{4.5}$$

This calculation also provided a means of calculating the average % heat loss of the test section.

The next step in calculating the bulk fluid temperatures at the desired locations was calculating the enthalpy at each location. This was done by using the test section inlet pressure and temperature, P_x, and the mass flow rate.

$$h_x = \frac{P_x}{\dot{M}} - h\left[T_{inlet}, P_{inlet}\right] \tag{4.6}$$

The enthalpy value from Equation 4.6, along with the inlet pressure, was then used to calculate the temperature at point x by using the EES temperature query function that uses enthalpy and pressure as input variables. Once the bulk fluid temperature at the point was known a local heat transfer coefficient was calculated by dividing the average surface heat flux by the difference of the wall temperature and the bulk fluid temperature. The Nusselt number could then be calculated by multiplying the heat transfer coefficient by the hydraulic diameter, and dividing by the thermal conductivity of the fluid. The thermal conductivity was calculated using the temperature of the bulk fluid at the location. Finally the Reynolds number was calculated using the hydraulic diameter.

$$\mathrm{Re}_{d_h} = \frac{U\rho D_h}{\mu} \tag{4.7}$$

Where the velocity (U) was calculated by multiplying the volumetric flow rate by the flow area, and the density and dynamic viscosity were calculated using the bulk fluid temperature at the location.

The turbulent flow regime data was fitted with a typical Nusselt number correlation for turbulent flow, as shown below.

$$Nu_d = C\,\mathrm{Re}_d^m\,\mathrm{Pr}^n \qquad (4.8)$$

The Prandtl number like all other fluid properties was calculated using the bulk fluid temperature. In order to estimate the exponent n, the turbulent data was plotted as $\log(Nu_d/Re_d^m)$ versus log Pr. This value of n was then set to .33, because this best fit the data while still staying within the bounds of previous correlations. With a known exponent n, the exponent m and coefficient C could then be calculated by plotting all the data as $\log(Nu_d/Pr^n)$ versus log Re_d.

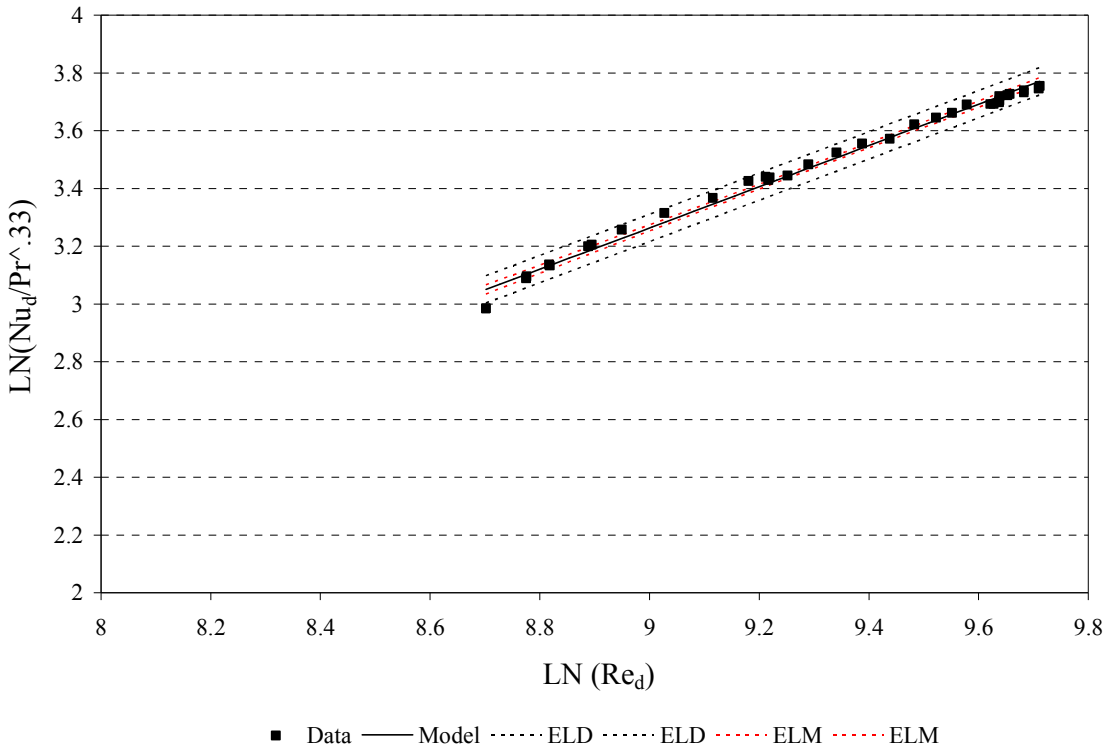

Figure 4.2: Plot of Exponential fit for Turbulent Data

CHAPTER V

RESULTS AND DISCUSSION

This chapter contains the presentation and discussion of experimental data obtained in this investigation. Section V.1 focuses on OFI experimental results, while Section V.2 focuses on Nusselt Number correlations.

5.1 Onset of Flow Instability

This OFI investigation produced a total of 12 experiments covering a range of exit pressures and heat fluxes. Appendix B lists the OFI conditions for all experiments conducted; the data include the inlet temperature, the exit pressure, the coolant mass flux, and the average surface heat flux. All 12 experiments used fully nitrogen-saturated water as the coolant, and the inlet temperature was fixed to within a few degrees of 25ºC. A correlation that covers a heat flux range of 0.729 – 2.236 MW/m^2 was developed using all 12 OFI data points. Within this section is a discussion of the OFI results obtained and the empirical correlations developed.

5.1.1 Effect of Surface Heat Flux on OFI

Figure 5.1 illustrates the effect of increasing surface heat flux on OFI. The experiments shown in Figure 5.1 had the inlet temperature and exit pressure held at 25ºC and 25 psig, respectively. The data shows that as the surface heat flux decreased, the mass flux at which OFI occurred also decreased. While no trend can be fitted to the data, it's clear that there is a positive correlation between surface heat flux and the mass flux at which OFI occurs.

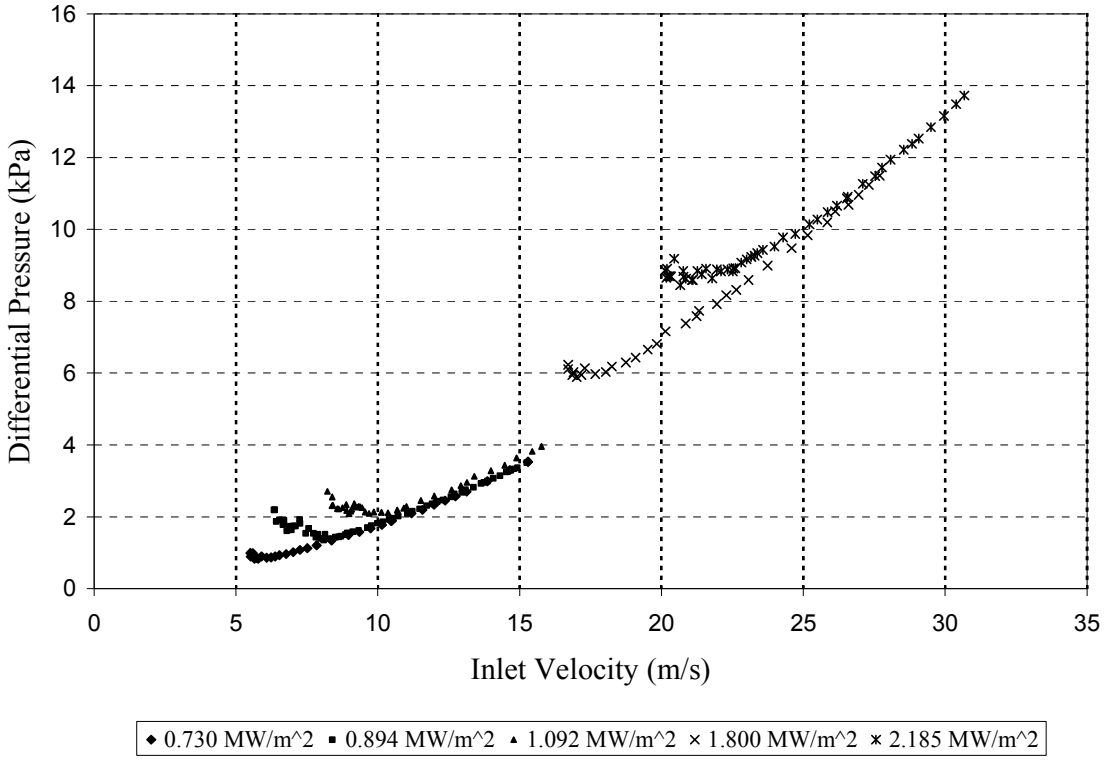

Figure 5.1: Effect of Changing Surface Heat Flux on the OFI Demand Curve

5.1.2 Effect of Exit Pressure on OFI

Figure 5.2 illustrates the effect of test section exit pressure on OFI. For the three experiments shown here the inlet temperature and heat flux were maintained at 25ºC and 1.5 MW/m^2, respectively. The data shows a negative correlation between exit pressure and the OFI mass flux. Exit pressure's effect is significant; going from 620 to 275 kPa increases the OFI mass flux by about 50%. However, like the correlation between surface heat flux and OFI mass flux, no trend can be accurately fitted to the data.

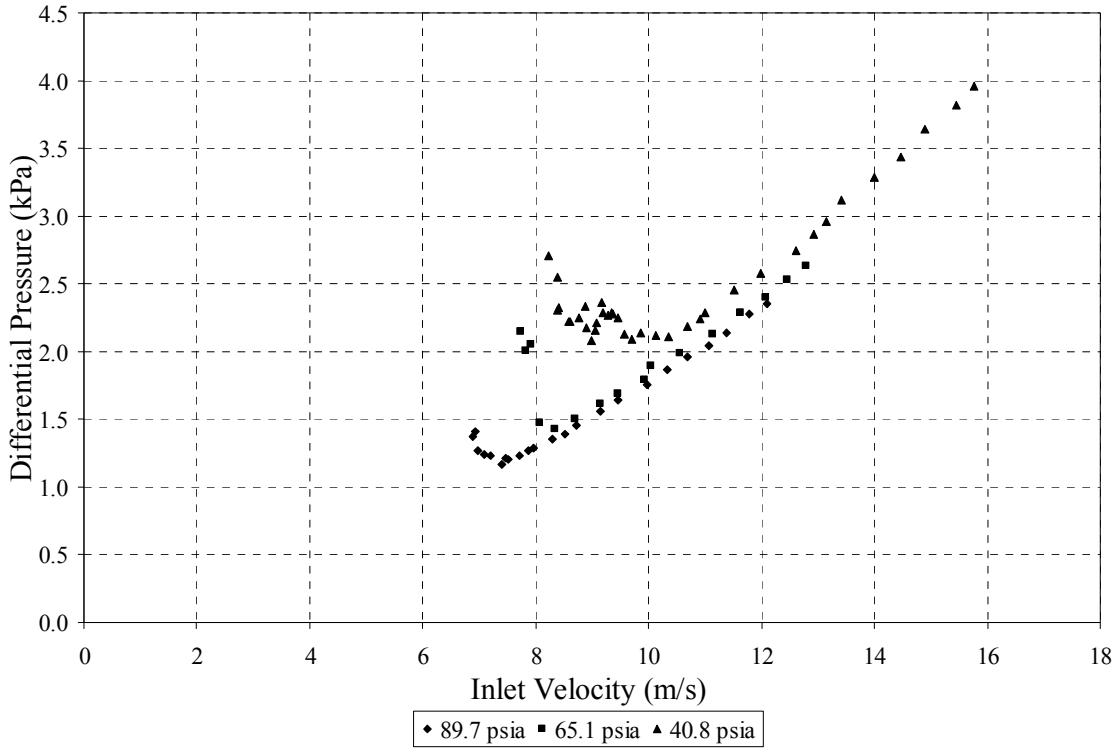

Figure 5.2: Effect of Changing Exit Pressure on the OFI Demand Curve

5.1.3 Comparison with Kennedy's OFI Model

Kennedy, et al. (1997) conducted OFI experiments using four test sections with two types of cross-sections, circular and microbundle interior subchannel. Based on the results of those experiments, the following OFI correlations were developed.

$$q''_{OFI} = 0.900 * q''_{sat} \pm 6.9\% \qquad (5.1)$$

$$G_{OFI} = 1.110 * G_{sat} \pm 6.3\% \qquad (5.2)$$

Figures 5.3 and 5.4 compare the OFI data obtained during this investigation against the correlations of Kennedy, et al. (1997). These figures show that the Kennedy correlations do not fit the data obtained in this investigation. It is clear that the flow characteristics vary between the circular cross-sections Kennedy used and the rectangular cross-sections, used in this investigation.

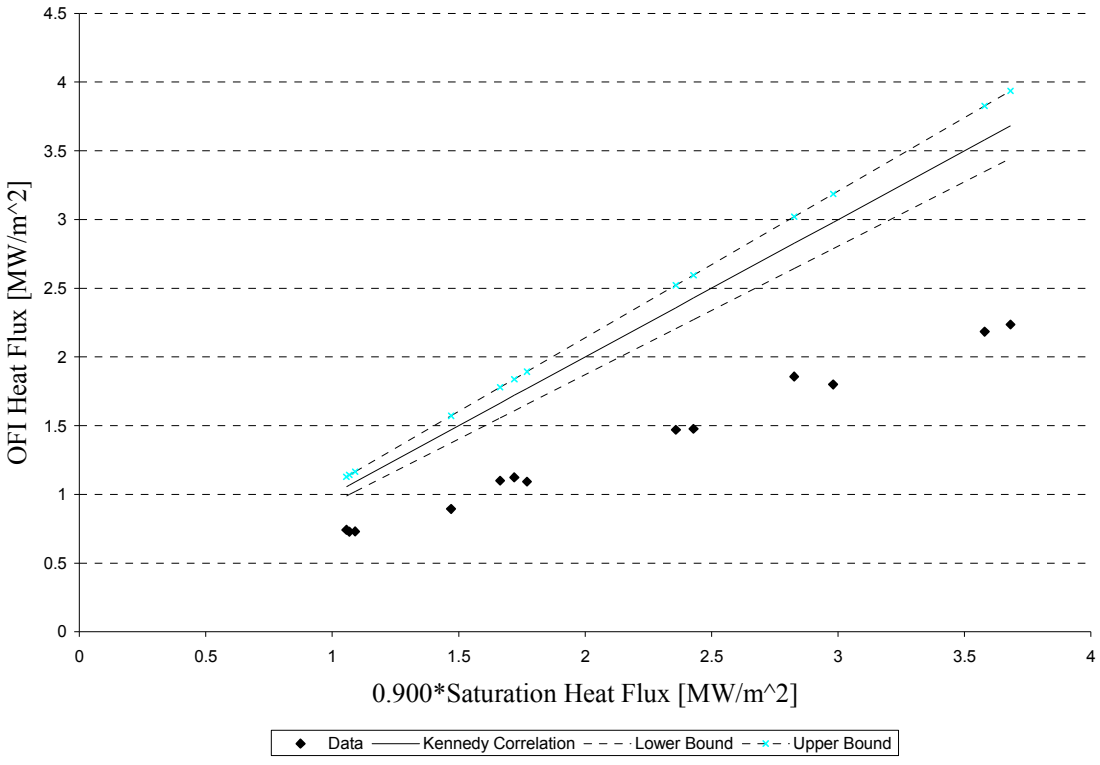

Figure 5.3: Comparison of OFI Heat Flux Data with Kennedy (1997) OFI Model

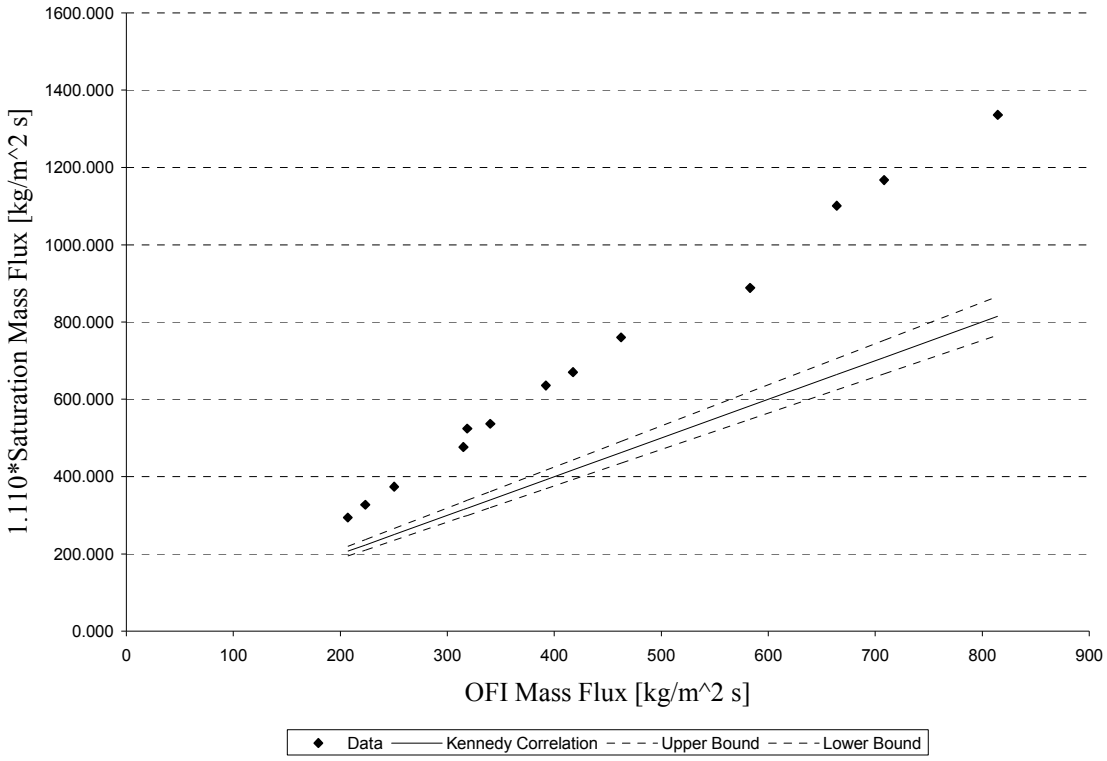

Figure 5.4: Comparison of OFI Mass Flux Data with Kennedy (1997) OFI Model

5.1.4 Development of OFI Correlation

As described in Section IV.7.2, with OFI mass flux, OFI heat flux, inlet enthalpy, heat loss, and exit pressure known for each experiment, the corresponding heat flux and mass flux that would lead to saturation at the test section exit were calculated using an energy balance:

$$G_{sat} = q''_{OFI} \frac{A_{heated}}{A_{flow}(h_f[P_{exit}] - h[T_{inlet}, P_{inlet}]} \tag{5.3}$$

$$q''_{sat} = G_{OFI} \frac{A_{flow}}{A_{heated}} \left(h_f[P_{exit}] - h[T_{inlet}, P_{inlet}]\right) \tag{5.4}$$

Based on the above energy balances, simple, linear correlations were developed for the OFI heat flux and mass flux as functions of saturation mass flux and heat flux, respectively. Using this approach, Kennedy, et al. (1997) developed correlations for OFI through circular microchannels. The following correlations developed in this investigation are for the narrow, rectangular cross section as described in Chapter III.

$$q''_{OFI} = 0.561 * q''_{sat} \pm 6.41\% \qquad (5.5)$$

$$G_{OFI} = 1.790 * G_{sat} \pm 7.96\% \qquad (5.6)$$

These linear correlations were developed by minimizing the sum of the squares of the absolute error (i.e., the difference between the experimental values and the predicted values). Using a 95% confidence level as a baseline, these correlations predict the OFI heat flux given a known mass flux within ± 6.41% and ± 7.96% for OFI mass flux given a known heat flux. The uncertainty ranges equal twice the standard deviation of the percent error between the raw OFI data and the prediction. Figures 5.5 and 5.6 compare predictions of the above correlations with the data. These correlations are only valid for the parameters covered during this investigation:

Heat Flux:	0.729 → 2.236 MW/m^2
Mass Flux:	295 → 1336 kg/m^2 sec
Inlet Temperature:	Room Temperature (25ºC)
Exit Pressure:	275 → 620 kPa
Non-Condensable Gas Content:	Saturated at T_{inlet} and P_{exit}
Coolant Channel Geometry:	Rectangular
Coolant Channel Gap Thickness:	1.1mm
Coolant Channel Aspect ratio:	11/100

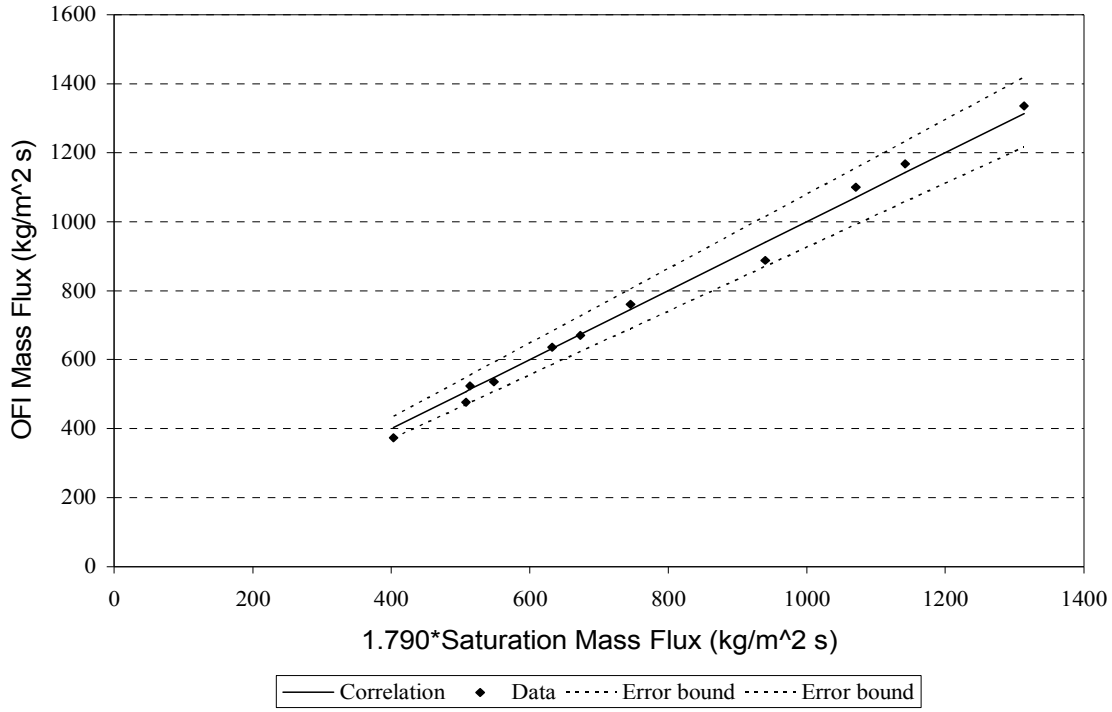

Figure 5.5: OFI Mass Flux Correlation

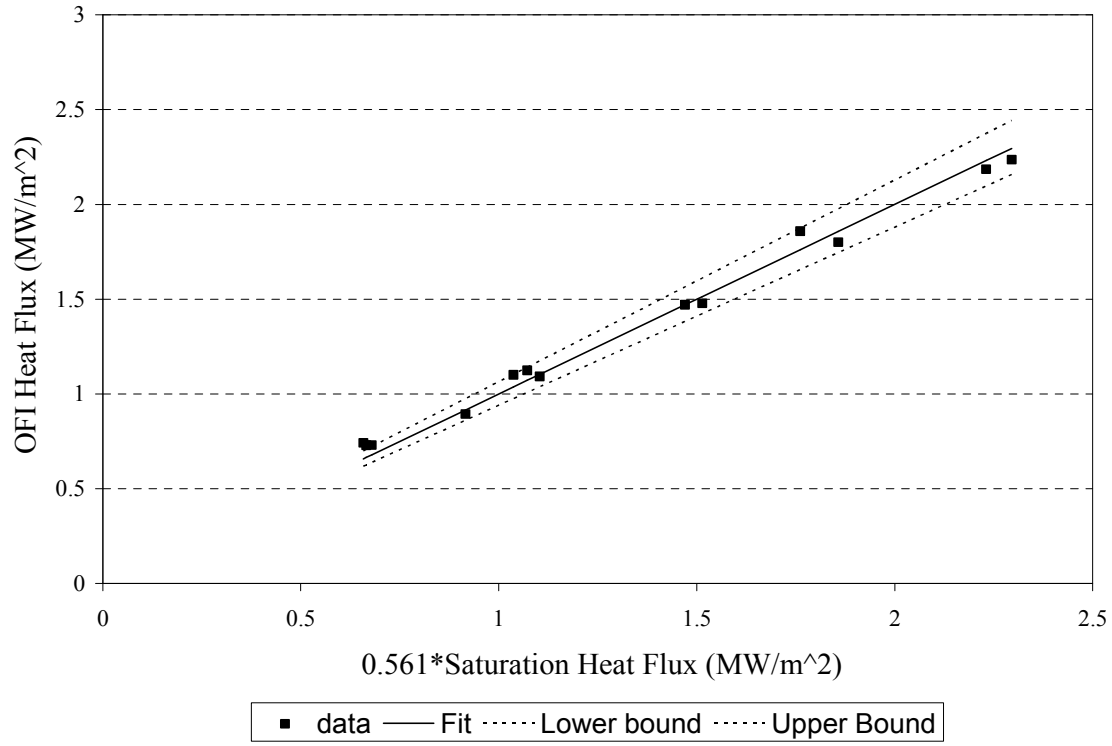

Figure 5.6: OFI Heat Flux Correlation

5.2 Nusselt Number

Figure 5.3 illustrates the Nusselt number as a function of Reynolds number data obtained in this investigation. Flow rates were chosen to cover both the laminar and turbulent flow regimes. The power was maintained at a low heat flux, preventing any flow regime changes due to vapor formation. The turbulent-laminar transition region is shown clearly between 3500 and 6000 Reynolds number.

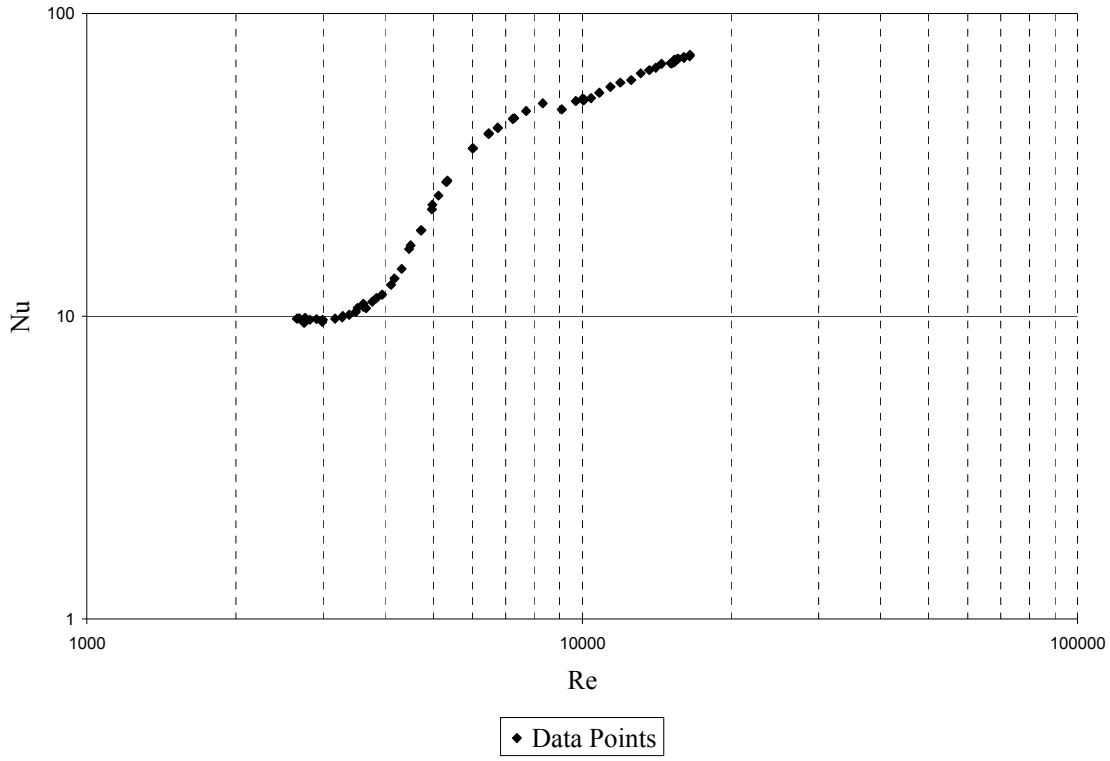

Figure 5.7: Plot of Nusselt Number versus Reynolds number

5.2.1 Turbulent flow

The turbulent flow regime analyzed in this investigation covered a range of 6000 to 17000 Re. For values lower than 6000 Re the flow began to transition and therefore it was impractical to include lower Reynold number data points in the turbulent flow correlation.

Many forced convection correlations for turbulent flow in large channels originate in the Colburn (1933) equation. One of these correlations is the widely used Dittus-Boelter (1936) correlation for turbulent flow in circular channels.

$$Nu_D = 0.023\,\mathrm{Re}_D^{0.8}\,\mathrm{Pr}^n$$

Where n = 0.4 for heating ($T_s > T_b$), n = 0.3 for cooling (Ts<Tm)

The correlation is valid for Reynolds numbers and Prandtl numbers in the ranges of $Re_D \geq 10^4$ and 0.7 – 100, respectively, and an L/D ratio larger than 60. The correlation is frequently used for turbulent flow in non-circular channels by using the hydraulic diameter in the Reynolds number rather than the diameter D. For this investigation the hydraulic diameter was calculated to be 1.842mm.

An alternate correlation for single-phase turbulent forced convection was suggested by Petukhov et al. (1973).

$$Nu = \frac{(f/8)*\mathrm{Re}\,\mathrm{Pr}}{K + 12.7*(f/8)^{1/2}\left(\mathrm{Pr}^{2/3}-1\right)}$$

Where

$$K = 1.07 + (900/\mathrm{Re}) - [0.63/(1+10*\mathrm{Pr})]$$

The recommended friction factor correlation is that of Filonenko (1954):

$$f = (1.82\log(\mathrm{Re}) - 1.64)^{-2}$$

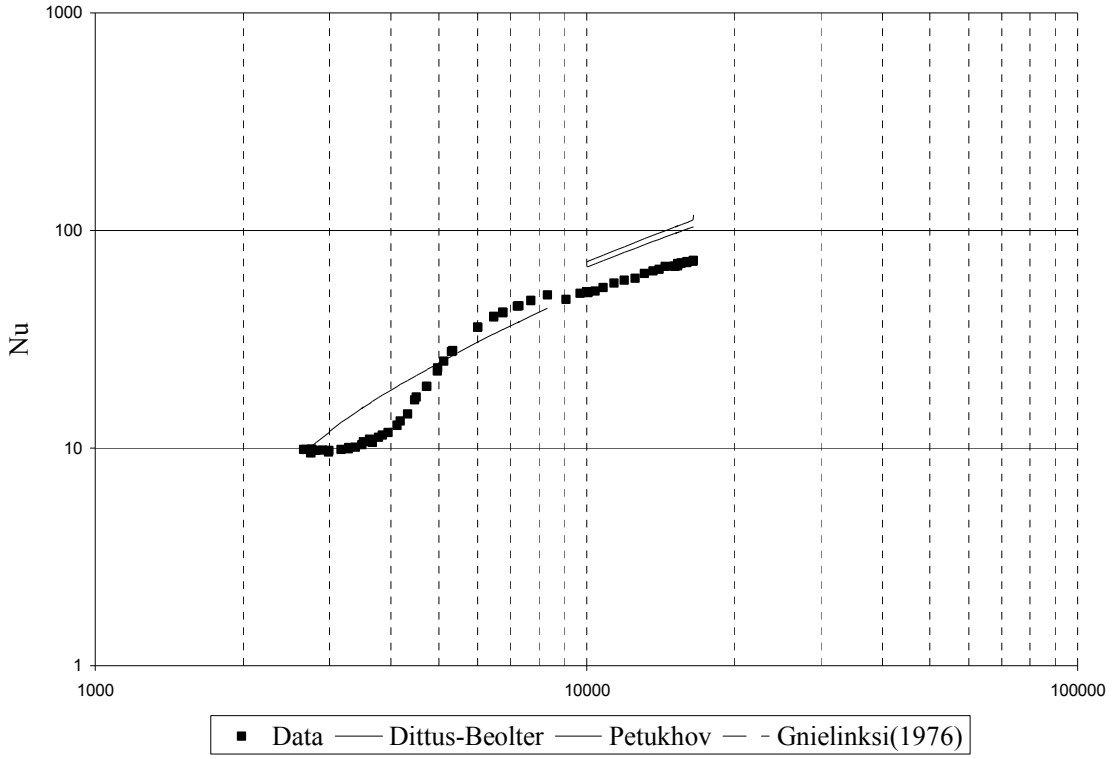

Figure 5.8: Comparison of Data to Turbulent flow correlations

The data suggests that the Nusselt number for the narrow rectangular cross-section is lower than traditional turbulent flow Nusselt number correlations. This is contradictory to the theory proposed by Adams (1999), who reported that the Nusselt number for turbulent flow in microchannels is higher than the values for large channels. However, Adams developed his theory on circular cross-sections, so it's possible that narrow rectangular slits hold different characteristics, as was the case in the OFI correlations.

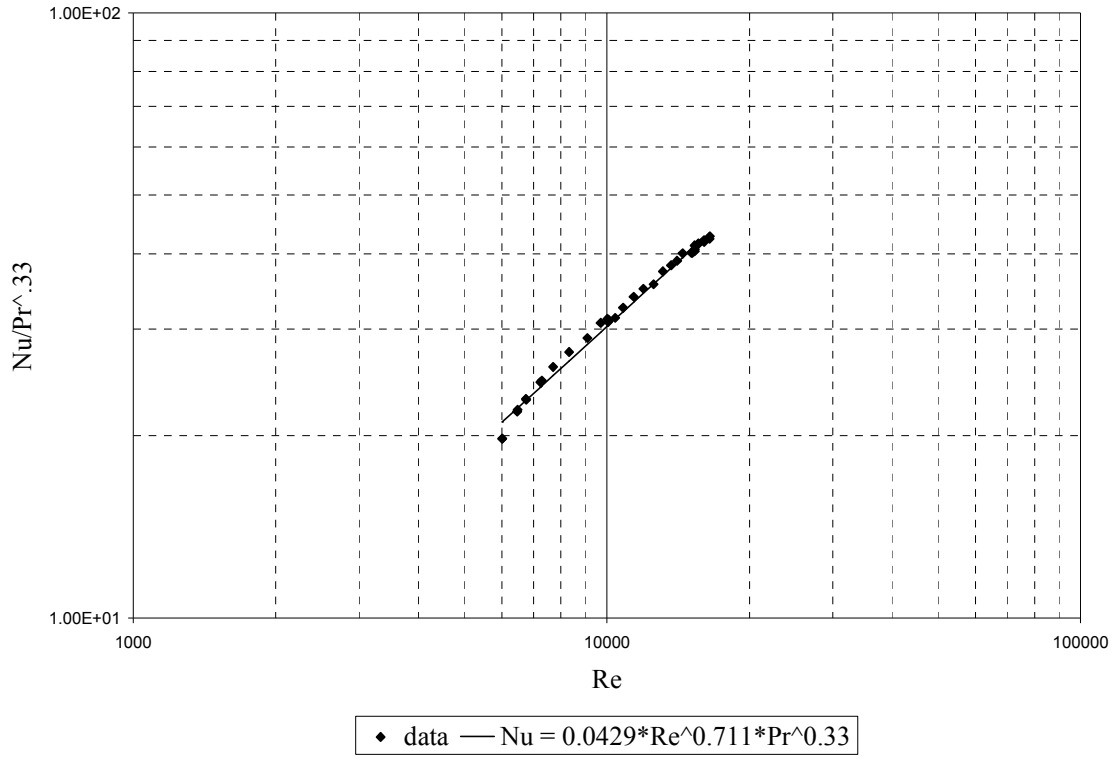

Figure 5.9: Plot of Nu/Pr^.33 versus Reynolds Number for Turbulent Flow Regime

The following turbulent correlation developed in this investigation is for the narrow, rectangular cross section as described in chapter III.

$$Nu_d = 0.0429\,\mathrm{Re}_d^{0.711}\,\mathrm{Pr}^{0.33} \pm 3.036\% \qquad (5.7)$$

This correlation was developed using the methods outlined in section IV.5.3. While the coefficient is significantly larger than traditional correlations, the Reynolds number exponent correlation is lower. The effect of the exponent is more significant than that of the coefficient. Therefore the Nusselt number prediction of the model is lower than that of traditional correlations.

5.2.2 Transitional and Laminar Flow

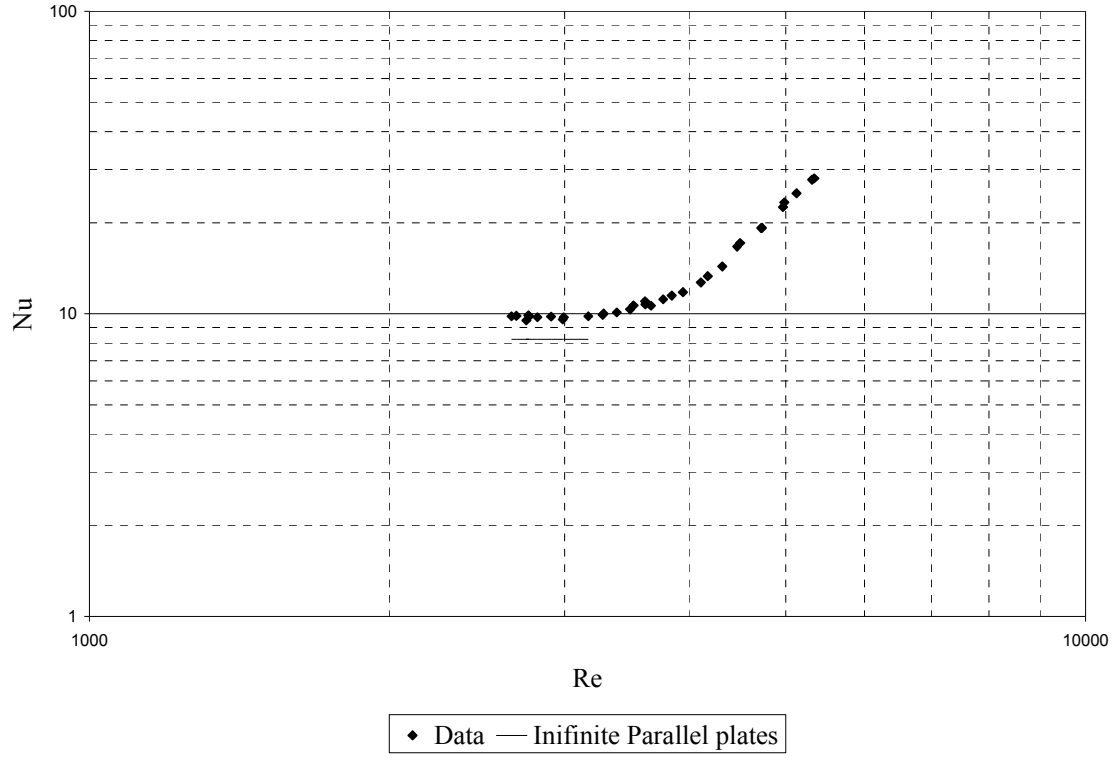

Figure 5.10: Plot of Nusselt Number versus Reynolds Number

Figure 5.9 shows a clear transition region towards fully developed laminar flow between 5500 and 3500 Reynolds number. This is higher than the traditional correlations that show the laminar region forming around 2100 Reynolds number. The Nusselt number in the fully developed laminar region converges to 9.75. This number is higher than the fully developed laminar Nusselt number for infinite parallel planes, 8.235, implying that for narrow rectangular slits the Nusselt number is slightly higher than traditional rectangular ducts. Additionally it's clear that the flow in rectangular ducts transitions to laminar flow at much higher Reynolds numbers.

CHAPTER VI

CONCLUSIONS

Ledinegg flow instability and heat transfer coefficient experiments were conducted with water flowing through a narrow, rectangular channel using the Georgia Tech Microchannel Test Facility. Subcooled water at a controlled flow rate, pressure, temperature, and dissolved non-condensable gas concentration was delivered to the rectangular test section. By running an electrical current through the test section making use of its electrical resistance, a constant heat flux was applied. A total of 13 OFI experiments and 3 heat transfer coefficient experiments were conducted in this investigation. The tables located in Appendices B and C provide all of the OFI and heat transfer coefficient data collected and used during this study.

6.1 OFI Correlations

1. With all other operating parameters constant, OFI occurred at higher mass fluxes as the surface heat flux applied to the test section was increased.
2. With all other operating parameters constant, OFI occurred at higher mass fluxes as the test section exit pressure was decreased.
3. The comparison of the correlations developed in this investigation with those of previous investigations show OFI tends to occur at higher mass fluxes in rectangular cross-sections as compared to circular cross-sections.

3. An OFI correlation was developed relating the heat flux required to cause bulk exit saturation of the working fluid with the heat flux required to initiate OFI. A second OFI correlation was developed for the coolant mass flux data.

$$q''_{OFI} = 0.561 * q''_{sat} \pm 6.41\% \qquad (6.1)$$

$$G_{OFI} = 1.790 * G_{sat} \pm 7.96\% \qquad (6.2)$$

The data fit both these correlations within a 95% (2σ) confidence level. The parameter ranges used to develop these correlations were:

Heat Flux:	0.729 → 2.236 MW/m^2
Mass Flux:	295 → 1336 kg/m^2 sec
Inlet Temperature:	Room Temperature (25ºC)
Exit Pressure:	275 → 620 kPa
Non-Condensable Gas Content:	Saturated at T_{inlet} and P_{exit}
Coolant Channel Geometry:	Rectangular
Coolant Channel Gap Thickness:	1.1mm
Coolant Channel Aspect ratio:	11/100

4. The models developed in previous investigations would be highly non-conservative when applied to the data found in this investigation.

APPENDIX A

EES ROUTINES

A.1 Heat Transfer Coefficient Routine

This Routine was used to calculate the bulk fluid temperature at the three locations of the wall thermocouples. The input variables included, bulk exit fluid temperature, bulk inlet fluid temperature, inlet fluid pressure, and bulk fluid flow rate. A uniform heat flux was assumed and therefore the power input before each location was determined using the ratio of partial length over total heated length.

```
P_in =(30+14.696)*convert(psi,kpa)
T_in =21.52
T_out = 38.46
Flow_2=28.21
rho_1 = DENSITY(Water,T=T_in,P=P_in)
Flow =flow_2*convert(gal/hr,m3/sec)
Mass_Flow = Flow* rho_1
Power = -Mass_Flow*(Enthalpy(Water,T=T_in,P=P_in) - Enthalpy(Water,T=T_out,P=P_in))
q1 = Power*(1.68/4.154)[kW]
q2 = Power*(2.391/4.154)[kW]
q3 = Power*((2.391+.771)/4.154)[kW]
H_in=Enthalpy(Water,T=T_in,P=P_in)
H_1 = q1/Mass_Flow + H_in
T_1 =Temperature(Water,P=P_in,h=H_1)
H_2 = q2/Mass_Flow + H_in
T_2=Temperature(Water,P=P_in,h=H_2)
Pr_1=Prandtl(Water,T=(T_1+T_2)/2,P=P_in)
H_3 =q3/Mass_Flow +H_in
T_3= Temperature(Water,P=P_in,h=H_3)
```

A.2 Expected Power Flux and Flow Rates for Saturation

This code was used to calculate the expected power fluxes and flow rates required to reach saturation. The input variables included inlet fluid pressure, bulk fluid flow rate, power input, and bulk inlet fluid temperature.

```
P_1 =25* convert(psi,pa) +101325
```

```
flow =7.839 *convert(gal/hr,m3/s)
Power =2.448
T_1 = 19.2
T_sat_2=T_sat(Water,P=P_1)
x_2=0
h_1=Enthalpy(Water,T=T_1,P=P_1)
h_2=Enthalpy(Water,T=T_sat_2,x=x_2)
rho_1=Density(Water,T=T_1,P=P_1)
Flow_expected = Power / ((h_2-h_1)*rho_1) * convert(m^3/s,gal/hr)
Power_expected = flow*(h_2-h_1)*rho_1
```

A.3 Calculated and Measured Power Input

This EES routine was used to calculate both the measured power input from the voltmeters and the calculated power input using an energy balance equation. The equation for VAC_SHUNT is the same as EQ 3.3.

```
VAC_TS = 2
VDC_TS = 5
VDC_SHUNT = 100
VAC_SHUNT = VDC_SHUNT * VAC_TS / VDC_TS
V_TS = SQRT(VAC_TS^2 + VDC_TS^2)
C_SHUNT = SQRT(VDC_SHUNT^2 + VAC_SHUNt^2)
Power = V_TS * C_SHUNT
T_in = 26.1
T_out =40.1
Flow = 44.3 * convert(gal/hr,m3/sec)
P_in = 25 * convert(psi,kpa)
h_in = Enthalpy(Water,T=T_in,P=P_in)
h_out = Enthalpy(Water,T=T_out,P=P_in)
rho_1 = Density(Water,T=T_in,P=P_in)
Power_calc= rho_1 * Flow *(h_out - h_in)
```

APPENDIX B

SUMMARY OF OFI EXPERIMENTAL DATA

The conditions corresponding to OFI for the 13 experiments conducted in this investigation are tabulated in Table B.1. The non-condensable gas content, gap width, inlet temperature, exit pressure, OFI mass flux, and OFI surface heat flux are all provided in Table B.1

Table B.1: OFI Experimental Data

Non-Condensable Gas Content	Gap Width	T_{inlet}	T_{outlet}	P_{exit} (absolute)	OFI Mass Flux	OFI Heat Flux
	(mm)	(ºC)	(ºC)	(kPA)	(kg/m^2 s)	(MW/m^2)
Nitrogen-Saturated	1.4	18.7	92	274	374.18	0.730
Nitrogen-Saturated	1.4	23.6	93	274	635.96	1.092
Nitrogen-Saturated	1.4	26.4	83	274	1100.73	1.800
Nitrogen-Saturated	1.4	27.5	84	274	1336.22	2.185
Nitrogen-Saturated	1.4	22.8	86	274	524.25	0.894
Nitrogen-Saturated	1.4	22.8	106	446	327.47	0.729
Nitrogen-Saturated	1.4	24.9	105	446	536.68	1.124
Nitrogen-Saturated	1.4	25.3	96	446	760.29	1.478
Nitrogen-Saturated	1.4	25.7	91	446	888.00	1.858
Nitrogen-Saturated	1.4	26.8	93	446	1167.27	2.236
Nitrogen-Saturated	1.4	23.2	120	618	294.53	0.742
Nitrogen-Saturated	1.4	26.6	115	618	476.62	1.101
Nitrogen-Saturated	1.4	25.6	108	618	670.35	1.471

APPENDIX C

SUMMARY OF HEAT TRANSFER COEFFICIENT DATA

All the data points used in developing the Nusselt number correlations are tabulated in Table C.1. The Reynolds number, bulk temperature 1, bulk temperate 2, the two wall temperatures, measured power, calculated power, power loss, and the nusselt number are provided.

Table C.1: Heat Transfer Coefficient Data

Reynolds	$T_{bulk\ 1}$	$T_{bulk\ 2}$		$T_{wall\ 1}$	$T_{wall\ 2}$		P_{rec}	P_{calc}	loss		Nu
	(ºC)	(ºC)		(ºC)	(ºC)		(kW)	(kW)	(%)		
16501	32.03	33.82		64.98	73.54		3.00	2.73	9.25%		72.9
16471	31.95	33.74		64.97	74.09		3.00	2.72	9.25%		72.3
16031	32.07	33.91		65.27	74.55		3.00	2.72	9.25%		71.8
16031	31.99	33.83		65.52	74.48		3.00	2.72	9.25%		71.3
15621	32.06	33.95		65.73	74.94		3.00	2.72	9.25%		70.9
15556	32.06	33.95		65.81	75.16		3.00	2.72	9.25%		70.6
15335	32.10	34.03		66.04	75.33		3.00	2.72	9.25%		70.3
15169	32.10	34.05		66.90	76.58		2.99	2.72	9.25%		68.4
15321	31.99	33.91		66.59	76.19		3.00	2.72	9.25%		68.9
15331	31.95	33.87		66.40	75.88		3.00	2.73	9.25%		69.4
15081	32.04	34.00		66.76	76.57		3.00	2.72	9.25%		68.5
14452	32.25	34.30		67.13	77.23		3.00	2.72	9.25%		68.2
14065	32.31	34.42		67.99	78.54		2.99	2.71	9.25%		66.2
13659	32.43	34.60		68.60	79.49		2.98	2.71	9.25%		65.0
13131	32.60	34.87		69.52	80.97		2.98	2.70	9.25%		63.4
12558	32.80	35.18		71.68	83.47		2.98	2.70	9.25%		60.3
11936	33.08	35.60		72.47	85.24		2.98	2.70	9.25%		59.1
11395	33.41	36.08		74.14	87.73		2.99	2.71	9.25%		57.2
10826	33.75	36.59		76.35	90.88		3.00	2.72	9.25%		54.7
10419	33.91	36.85		77.77	92.97		2.97	2.70	9.25%		52.5
10064	34.09	37.13		78.32	93.92		2.95	2.68	9.25%		51.6
10086	34.10	37.45		79.27	94.63		2.96	2.74	7.33%		52.0
10013	33.97	37.01		78.65	94.00		2.94	2.73	7.17%		52.3
9705	34.23	37.38		80.09	95.81		2.94	2.76	6.16%		51.4
9094	34.88	38.31		84.37	100.91		2.94	2.79	5.32%		48.2
8326	23.55	24.42		42.82	49.91		1.18	1.12	4.67%		50.5
7704	23.76	24.70		44.06	51.61		1.18	1.12	5.27%		47.6
7244	23.94	24.95		45.42	53.15		1.18	1.11	5.83%		44.9
7292	23.92	24.93		45.43	53.21		1.17	1.12	4.84%		45.1

Table C.1 (continued)

6747	24.16	25.25		47.26	54.89		1.18	1.11	5.88%		42.0
6757	24.18	25.27		47.53	55.05		1.18	1.11	5.52%		41.8
6469	24.36	25.50		49.19	56.17		1.17	1.11	5.14%		39.9
6477	24.37	25.52		49.05	56.12		1.17	1.12	4.87%		40.2
6014	24.73	25.98		54.90	57.35		1.17	1.12	4.22%		35.9
6014	24.74	25.99		54.90	57.30		1.17	1.12	4.45%		35.8
5342	25.43	26.90		76.69	60.02		1.17	1.15	1.44%		28.0
5316	25.49	26.97		79.00	59.74		1.17	1.15	1.28%		27.7
5126	25.75	27.32		85.39	64.18		1.16	1.16	-0.08%		25.0
4985	26.07	27.73		90.86	68.17		1.16	1.19	-2.60%		23.4
4969	26.06	27.72		92.01	69.79		1.16	1.19	-2.21%		22.6
4734	26.37	28.12		96.72	80.38		1.16	1.18	-2.08%		19.2
4724	26.34	28.06		95.76	79.85		1.15	1.17	-0.92%		19.2
4502	26.50	28.28		98.77	87.01		1.15	1.14	1.49%		17.1
4470	26.71	28.53		100.17	90.88		1.15	1.15	-0.14%		16.7
4319	26.50	28.25		102.70	99.29		1.15	1.08	6.46%		14.3
4177	26.55	28.29		103.41	103.75		1.15	1.04	9.53%		13.3
4110	26.48	28.20		104.54	105.42		1.15	1.01	12.35%		12.7
3943	26.63	28.39		106.07	112.13		1.15	0.98	14.51%		11.8
3843	26.72	28.50		106.70	113.25		1.15	0.97	15.58%		11.5
3768	26.78	28.57		107.61	114.47		1.15	0.95	16.93%		11.2
3662	26.79	28.57		108.63	116.33		1.15	0.92	19.62%		10.6
3614	27.05	28.90		109.59	117.78		1.15	0.94	17.87%		10.8
3613	27.16	29.05		109.12	117.15		1.15	0.96	16.40%		11.0
3489	27.23	29.12		110.97	120.04		1.15	0.93	19.33%		10.3
3518	27.35	29.29		110.41	119.05		1.15	0.94	17.75%		10.6
3384	27.43	29.36		111.82	121.10		1.15	0.91	20.44%		10.1
3275	27.67	29.67		113.06	122.83		1.15	0.91	20.76%		9.9
3283	27.78	29.81		113.50	123.38		1.15	0.92	19.68%		10.0
3168	28.08	30.19		114.97	125.42		1.15	0.92	19.97%		9.8
2993	28.89	31.19		117.00	128.35		1.15	0.93	19.06%		9.7
2986	28.88	31.16		117.41	128.81		1.15	0.92	19.91%		9.6
2906	29.49	31.93		118.53	130.06		1.14	0.94	17.49%		9.8
2817	29.93	32.51		119.91	132.14		1.14	0.95	16.61%		9.7
2745	29.97	32.55		119.86	132.15		1.14	0.93	18.73%		9.5
2764	30.39	33.09		120.69	133.14		1.14	0.96	15.70%		9.8
2759	30.45	33.17		120.93	133.31		1.14	0.97	15.14%		9.9
2684	30.90	33.74		122.30	135.06		1.14	0.98	14.29%		9.8
2654	31.08	33.97		122.67	135.52		1.14	0.98	14.27%		9.8

APPENDIX D

OFI ERROR ANALYSIS

The OFI mass flux error analysis is presented within this appendix. The following examination is modeled after Stoddard's (2000) analysis.

D.1 Mass Flux Error Analysis

Mass flux is a function of the coolant mass flowrate and the cross-sectional area of the test section.

$$G = \frac{\dot{m}}{A_{cs}} \tag{B.1}$$

In order to calculate the coolant mass flux variance the following error propagation formula can be used.

$$\sigma_G^2 = \left(\frac{\partial G}{\partial \dot{m}}\right)^2 \sigma_{\dot{m}}^2 + \left(\frac{\partial G}{\partial A_{cs}}\right)^2 \sigma_{A_{cs}}^2 \tag{B.2}$$

Simple calculus analysis yields the following expressions for the partial derivatives.

$$\frac{\partial G}{\partial \dot{m}} = \frac{1}{A_{cs}} \text{ and } \frac{\partial G}{\partial A_{cs}} = -\frac{\dot{m}}{A_{cs}^2} \tag{B.3}$$

In order to calculate the variance of the coolant mass flowrate and the cross-sectional area, they had to be expanded into known components whose variances could be calculated.

Mass Flow rate ($\dot{m}$) can be expressed as a function of Volumetric flowrate ($\dot{V}$) and coolant density (ρ).

$$\dot{m} = \dot{V}\rho \tag{B.4}$$

The inlet temperature doesn't vary significantly; therefore the variance of the density can be set to zero. This yields the following equation for the variance of coolant mass flow rate.

$$\sigma_{\dot{m}}^2 = \left(\frac{\partial \dot{m}}{\partial \dot{V}}\right)\sigma_{\dot{V}}^2 \tag{B.5}$$

Where

$$\frac{\partial \dot{m}}{\partial \dot{V}} = \rho$$

The variance of the volumetric flowrate at OFI, measured using by FT-08 and FT-03 liquid flow transducers manufactured by EG&G/FTI, was calculated by summing the squares of the individual errors. There were a total of four errors related with the volumetric flowrate.

The first two errors were a result of the dead weight method used for calibrating the flowmeters. The mass scale used to calibrate the flowmeters was accurate to .02 kg, and the minimum weight used 2kg and, therefore, the uncertainty for the mass measurement was 1%. The stopwatch used to calibrate the flowmeters was accurate to 1 second and the minimum time interval used was one minute and, therefore, the uncertainty for the mass measurement was 1.67%. The third error associated with the volumetric flowrate was the standard error of the regression calibration curve. This error was .064137 gallons/hr for the FT-03 transducer, and .25591 gallons/hr for the FT-08 transducer. Correspondingly the two transducers had minimum flowrates of 5 gallons/hr and 15 gallons/hr, respectively. This yielded uncertainties of 1.28% and 1.71% for the FT-03 and FT-08 transducers, respectively. Most of the experiments had flow through by the FT-03 and FT-08 paths; therefore the higher uncertainty of 1.71% was applied to all the data.

The final uncertainty of the volumetric flowrate was associated with the precision error in choosing the correct OFI point. As described in Chapter IV, the OFI point was chosen to be the flowrate (gallon/hr) associated with the smallest pressure drop (kPa) through the test section. In order to quantify the error associated with this method, the data points around the OFI point were fit with both a quadratic and a cubic fit. A plot of the quadratic fit to the data set with the highest error (50 psig exit pressure, 25ºC inlet temperature, 1.5 MW/m^2) is located in Figure B.1.

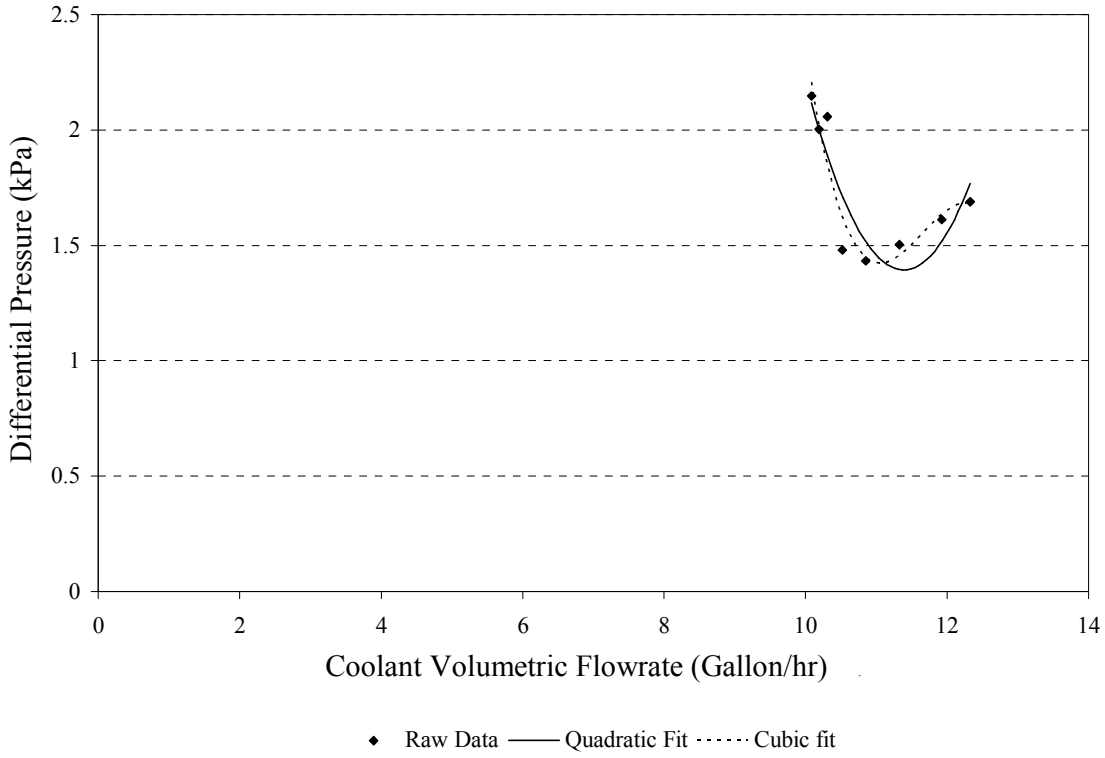

Figure B.1: Fits to OFI Demand Curve

The OFI points for both fits were calculated by taking the derivates of the formulas and setting them to zero. For the 2nd and 3rd order fits, the respective coolant volumetric flowrates were 11.39 and 11.06 gal/hr for the minimum differential pressures. The flowrate value corresponding to the data point with the lowest differential pressure was 10.80 gallons/hr. The 2nd order fit was used to calculate the precision uncertainty because it had the largest discrepancy.

$$u_4 = \frac{11.39 - 10.8}{10.8} = .0543 = 5.43\%$$

The squares of all four uncertainties were added in order to develop the error estimate for the volumetric flowrate at OFI.

Table D.1: Summary of Volumetric Flowrate Uncertainties at OFI

	Error Type	Uncertainty	Uncertainty^2
u_1	Bias	1%	1.000 E - 4
u_2	Bias	1.67%	2.789 E - 4
u_3	Bias	1.71%	2.924 E - 4
u_4	Precision	5.43%	2.948 E – 3
Sum		6.02%	3.620 E - 3

With the variance of the Volumetric Flowrate now known, all the values for Equation B.5 are known. This leaves the variance of the test section's cross sectional area as the final unknown in Equation B.2. This cross sectional area is a function of the test section's depth (D) and width (W).

$$A_{cs} = D * W + 2\pi\left(\frac{D}{2}\right)^2 \tag{B.6}$$

From Equation B.6 the variance of the test section cross sectional area can be expressed in the following manner.

$$\sigma_{A_{cs}}^2 = \left(\frac{\partial A_{cs}}{\partial D}\right)^2 \sigma_D^2 + \left(\frac{\partial A_{cs}}{\partial W}\right)^2 \sigma_W^2 \tag{B.7}$$

Where:

$$\frac{\partial A_{cs}}{\partial D} = W + 2\pi D \quad \text{and} \quad \frac{\partial A_{cs}}{\partial W} = D \tag{B.8}$$

The depth and width of the test section were both measured using a Max-Cal Caliper. The tolerance of the Max-Cal Caliper is .001 inch = .00254 cm. The test section's depth

and width were .13719 and 1.237 cm, respectively. Therefore, the respective uncertainty biases of the depth and width were 1.8% and .2%.

Finally, combining Equations B.2 through B.8 yielded the following equation for the coolant mass flux variance.

$$\sigma_G^2 = \left(\frac{1}{A_{cs}}\right)^2 \left[\rho^2 \sigma_{\dot{V}}^2 + \dot{m}^2 \left[(W + 2\pi D)^2 \sigma_D^2 + D^2 \sigma_W^2\right]\right] \qquad \text{(B.8)}$$

D.2 Heat Flux Error Analysis

The heat flux can be calculated as a function of the power applied to the test section and the test section heated area.

$$Q'' = \frac{Q_{total}}{A_s} \tag{B.9}$$

The variance of the surface heat flux can be expressed by the following error propagation formula.

$$\sigma_{Q''}^2 = \left(\frac{\partial Q''}{\partial Q_{total}}\right)^2 \sigma_{Q_{total}}^2 + \left(\frac{\partial Q''}{\partial A_s}\right)^2 \sigma_{A_s}^2 \tag{B.10}$$

where

$$\frac{\partial Q''}{\partial Q_{in}} = \frac{\partial Q''}{\partial Q_{out}} = \frac{1}{A_s} \text{ and } \frac{\partial Q''}{\partial A_s} = -\frac{(Q_{in} + Q_{out})}{A_s^2} = -\frac{Q_{total}}{A_s^2}$$

The variance of the power level at OFI was calculated as the sum of the squares of the individual bias errors and precision errors associated with the measurement. The OFI experiments measured the power level using redundant sensors. Since only the total power level reading supplied by the DC and AC wattmeters were used for analysis, only the tolerances of these wattmeters were considered in this error analysis.

APPENDIX E

CALIBRATION METHODS

E.1 Turbine Flowmeters

One of the most important instruments to calibrate correctly was the turbine flowmeters (Components 3 and 4). The volumetric flow was critical for calculating both the OFI and Nusselt number correlations. In order to calibrate the flowmeters the pump inlet was first isolated from the rest of the system by closing the Degassing tank isolation valve (Component Q) and the pump bypass valve (Component E). Next, the exit line from the test section was disconnected from the system heat exchanger (Component P) and was led to an empty bucket. Finally, the system drain valve (Component S) was connected to a large bucket of water. The system, no longer being self-contained, was now prepped for calibrating the flowmeters. As described in Appendix D, a stop watch accurate to one second was used to measure the time for each calibration measurement. A mass scale accurate to 10 grams was used to measure the total weight of water that passed through the flowmeter during each calibration measurement. Below the results of the calibrations for both turbine flowmeters are listed.

Table E.1: Calibration Data for Liquid Flow Transducer FT-03

FT-03			
Weight	Time	Reading	Volumetric Flow Rate
(kg)	(s)	(VDC)	(gal/hr)
0.3	117.8	0.347	2.10
0.5	107.3	0.694	4.00
0.5	99.6	0.860	4.91
0.6	70.1	1.570	8.16
1.0	93.5	1.910	10.20
1.3	99.1	2.480	12.51
1.7	106.9	3.068	15.17
1.1	59.5	3.500	17.63
1.6	72.9	4.200	20.94

$$\dot{V} = (0.6281 + 4.8302 * V_{\mathrm{Re}ading}) \pm 5.89\% \qquad \text{(E.1)}$$

Table E.2: Calibration Data for Liquid Flow Transducer FT-08 (Low Flow)

FT-08 (low flow)			
Weight	Time	Reading	Volumetric Flow Rate
(kg)	(s)	(VDC)	(gal/hr)
1.7	148.0	0.000	10.96
1.6	89.0	0.139	17.15
1.7	72.0	0.210	22.52
1.7	62.0	0.252	26.15
1.9	62.0	0.289	29.23
2.3	64.0	0.347	34.28
2.3	53.0	0.421	41.39

$$\dot{V} = 10.444 + 40.208 * V_{reading} + 80.948 * V_{reading}^{2} \pm 4.10\% \qquad \text{(E.2)}$$

Table E.3: Calibration Data for Liquid Flow Transducers FT-08 (High Flow)

FT-08 (high flow)			
Weight	Time	Reading	Volumetric Flow Rate
(kg)	(s)	(VDC)	(gal/hr)
2.0	62.0	0.310	30.77
3.5	65.4	0.518	51.04
3.5	45.1	0.768	74.04
4.3	47.1	0.907	87.14
4.1	40.3	0.994	95.98
4.5	41.6	1.067	103.11
3.9	33.7	1.160	110.52

$$\dot{V} = 1.780 + 95.127 * V_{reading} - 0.768 * V_{reading}^2 \pm 0.3\% \qquad \text{(E.3)}$$

REFERENCES

Adams, T.M., Ghiaasiaan, S.M. and Abdel-Kahlik, S.I., 1999, "Effect of Dissolved Noncondensables on Hydrodynamics of Channels Subject to Liquid Forced Convetction," *J. Enhanced Heat Transfer 6,* pp. 395-403.

Ahmad, S.Y., 1970, "Axial Distribution of Bulk Temperature and Void Fraction in a Heated channel with Inlet Subcooling," *J. Heat Transfer*, Vol. 92, pp. 595-609.

Arpaci, V. S., 1997, "Microscales of Turbulent Heat and Mass Trasnfer," *Advances in Heat Transfer*, Vol. 30, pp. 1-87.

Bankoff, S.G., Lee, S.C., and Knaani, A., 1991, "Literature Review on Forced-Convection Subcooled Nucleate Boiling," Westinghouse Savannah River Company Report WSRC-TR-91-98, Evanston, IL.

Bejan, A., 1984, *Convection Heat Transfer*, John Wiley and Sons, New York.

Bergles, A. E. and Rosenow, W. M., 1992, "The influence of Temperature Difference on the Turbulent Forced Convection Heating of Water," *J. Heat Transfer*, Vol. 85, pp. 268-270.

Bergles, A.E., 1977, "Review of Instabilities in Two-Phase Systems," in Two-Phase Flow and Heat Transfer, S. Kakac and F. Mayinger, Vol. 2, pp. 383-422, Hemisphere, Washington, D.C.

Bergles, A.E. and Rohsenow, W.M., 1964, "The Determination of Forced Convective Surface Boiling Heat Transfer," *J. Heat Transfer*, Vol. 86, pp.365-372.

Blasick, A.M., 1999, "Onset of Flow Instability in Heated, Horizontal Annuli," Georgia Institute of Technology Masters Thesis.

Boure, J.A., Bergles, A.E., and Ton, L.S., 1973, "Review of Two-Phase Flow Instability," *Nuclear Engineering Design*, Vol. 25, pp.1665-192.

Bowring, R.W., 1962, "Physical Model Based on Bubble Detachment and Calculation of Steam Voidage in the Subcooled Region of a Heated Channel," HBR-10, Institued for Atomenergi, Halden, Norway.

Bowring, R.W., 1972, "A Simple but Accurate Round Tube, Uniform Heat Flux, Dryout Correlation Over the Pressure Range 0.7 – 17 MW/m^2 (100 – 2500 psia)," AEEW-RR789, UKAEA.

Brauner, N., 1990, "The Relation Between Two-Phase Flow Under Reduced Gravity and Earth Experiments," *Int. Comm. Heat Mass Transfer*, Vol. 17, pp.271-282.

Caira, M., Caruso, G., and Naviglio, A., 1993, "Requirements of High Heat Flux for Fusion Reactor Components: Revised Models and Correlations Predict Critical Heat Flux in Subcooled Flow Boiling," Proc. 1993 National Heat Transfer Conf., Atlanta, GA, p. 383, American Nuclear Society.

Chen, J. C., 1963, "A Correlation for Boiling Heat Transfer to Saturated Liquids in Convective Flow," ASMW Paper No. 63-HT-34.

Choi, S. B., Barron, R.F. and Warrington, R.)., 1991, "Fluid Flow and Heat Transfer in Microtubes," Proceedings, ASME 1991 Winter Annual Meeting, DSC-Vol. 32, pp. 123-134.

Collier, J.G., 1972, "Convective Boiling and Condesnation," McGraw-Hill, London, pp. 382-40-6

Dix, G.E., 1971, "Vapor Void Fraction for Forced Convection with Subcooled Boiling at Low Flow Rates," Ph.D. Thesis, University of California, Berkeley, CA.

Evangelisti, R. and Lupoli, P., 1969, "The Void Fraction in an Annular Channel at Atmospheric Pressure," *Int. J. Heat Transfer*, Vol. 12, pp. 699=711.

Fried, L., "Pressure Drop and Heat Transfer for Two-Phase Two-Component Flow," 1954, Chem. Eng. Prog. Symp. Series – Heat Transfer- Research Studies for 1954, Vol. 50 (9), p. 47.

Ghiaasiaan, S.M. and Abdel-Khalik, S.I., 2001, "Two-Phase flow in Microchannels," *Advances in Heat Transfer*, Academic Press, Vol. 34, pp. 145 – 254.

Gnielinski, V., 1976, "New Equations for Heat and Mass Transfer in Turbulent Pipe and Channel Flow," *Int. Chem. Eng.*, Vol. 16 (2), 359-368.

Griffith, P., Clark, J.A., and Rohsenow, W.M., 1968, "Void Volume in Subcooled Boiling," ASME Paper 58-HT-19.

Groeneveld, D.C. and Snoek, C.W., 1986, "A Comprehensive Examination of Heat Transfer Correlations Suitable for Reactor Safety Analysis," Multiphase Science Technology, Hewitt, g.F., Delhaye, J.M., Zuber, N., Eds., Vol. 2, pp. 181-274, Hemisphere, Washington, D.C.

Hinze, J. O., 1975, "Turbulence," 2nd Ed., McGraw-Hill, New York.

Inaska, F., Nariai, H., and Shimura, t., 1989, "Pressure Drops in Subcooled Flow Boiling in Narrow Tubes," Heat Transfer, Japanese Research, Vol., 18, pp. 70-82.

Ishii, M., 1976, "Study of Flow Instabilities in Two-Phase Mixtures," Argonne National laboratory Report, ANL-76-23.

Kakac, S., Shaw, R. K. and Aung, W., 1987, *Handbook of Single-Phase Convective Heat Transfer*, John Wiley and Sons, New York.

Kandlikar, S. G., shoji, M., Dhir, W. K., Handbook of Phase Change: Boiling Condensation," Philadelphia, PA: Taylor & Francis, c1999.

Kays, W. M. and Crawford, B., 1985, "Convective Heat and Mass Transfer," McGraw-Hill, New York.

Kennedy, J.E., Roach , G.M., Dowling, M.F., Jeter, S.M., Ghiaasiaan, S.M., and Abdel-Khalik, S.I., 1997, "Onset of Flow Instability in Uniformly-Heated Microchannels," Georgia Institute of Technology Final Report, submitted to Westinghouse Savannah River Company.

Klein, S., 1992-2003, "Engineering Equation Solver," F-Chart Software, Madison, WI.

Kurdirka, A. A., 1966, "Two-Phase Convective Heat Transfer," *Chem. and Proc. Eng.,* pp. 43-64.

Lahey, R.T., and Moody, F.J., 1979, the Thermal-Hydraulics of a Boiling Water Nuclear Reactor, Second Edition, American Nuclear Society, LaGrange Park, IL.

Levy, S., Fuller, R. A. and Niemi, R. O., 1959, "Heat Transfer to Water in Thin Rectangular Channels," *Journal of Heat Transfer,* Vol. 81 (2), pp. 129-143.

Levy, S., 1967, "forced Convection Subcooled Boiling: Prediction of Vapor Volumetric Fraction," *Int. J. Heat Mass Transfer,* Vol. 10, pp. 951-965.

Mandhane, J.M., Gregory, G. A. and Aziz K., 1974, "A Flow Pattern Map for Gas-Liquid Flow in Horizontal Pipes," *Int. J. Multiphase Flow*, Vol. 1 pp. 537-553.

McBeth, R.V., 1956-66, "An Appraisal of Forced Convection Burnout Data," Proc. Inst. Mech. Eng., Vol. 180, pp.47-48.

McBeth, R.V., and Thompson, B., 1964, "Boiling Water Heat Transfer Burnout in Uniformly Heated Round Tubes: A Compilation of World Data with Accurate Correlations," UKAE report AEEW-R 356, Winfrith, England.

Peng, X.F and Wang, B.X., 1993, "Forced Convection and Flow Boiling Heat Transfer for Liquid Flowing Through Microchannels," *Int. J. Heat Mass Transfer*, Vol. 36, pp. 3421-3427.

Peng, X. F., Wang, B. X., Peterson, G. P. and MA, H. B., 1995, "Experimental Investigation of Heat Transfer in Flat Plates with Rectangular Microchannels," *Int. J. Heat and Mass Transfer*, Vol. 38 (1), pp. 127-137.

Peng, X. F., and Peterson, G. P., "The Effect of Thermofluid and Geometrical Parameters on Convection of Liquids through Rectangular Microchannels," *Int. J. Heat and Mass Transfer,* Vol. 38 (4), pp. 755-758.

Phillips, R. J., 1990, "Microelectronic Heat Sinks," Chapter 3 of advances in Thermal Modeling of Electronic Components, Volume 2, A. Bar-Cohen and A. D. Kraus, ed., ASME Press, New York.

Roach, G.M., 1998, "Onset of flow Instability and Critical Heat Flux in Uniformly-Heated Microchannels," Georgia Institute of Technology Masters Thesis.

Saha, P. and Zuber, N., 1974, "Point of Net Vapor Generation and Vapor Void Fraction in Subcooled Boiling," Proc. Fifth Int. Heat Transfer Conf., Tokyo, Japan.

Schlichting, H., 1968, "Boundary Layer theory," McGraw-Hill, New York.

Shah, M. M., 1981, "Generalized Prediction of Heat Transfer During Two Component Gas-Liquid Flow in Tubes and Other Channels," AIChE Symposium Series, 208, Vol. 77, pp. 140-151.

Suo, M., and Griffith, P., 1964, "Two-Phase Flow in Capillary Tubes," J. Basic Eng., pp. 576-582.

Staub, F.W., 1968, "The Void Fraction in Subcooled Boiling: Prediction of the Initial Point of Net Vapor Generation," J. Heat Transfer, Vol. 90, pp. 151-157.

Stoddard, R.M., Blasick, A.M., Dowling, M.F., Abdel-Khalik, S.I., Ghiaasiaan, S.M., and Jeter, S.M., 2000, "OFI and CHF Database for APT Tungsten Target Annuli," Georgia Institute of Technology Final Report, submitted to General Atomics.

Thom, J.R.S., Walker, W.M., Fallon, T.A., and Reising, G.F.S., 1966, "Boiling in Subcooled Water During Flow in Tubes and Annuli," Proc. Inst. Mech. Eng., 3C180.

Todreas, N.E. and Kazimi, M.S., 1990, "*Nuclear Systems I*," Hemisphere, New York.

Tong, L. S., Tang, Y. S. 1997, "Boiling Heat Transfer and Two-Phase Flow," Washington, D.C. : Taylor & Francis, c1997.

Vivay, M. M., Aggour, M. A. and Sims, G. E., 1982, "A Correlation of Mean Heat-Transfer Coefficients for Two-Phase Two-Component Flow in a Vertical Tube," Proceedings, 7th Int. Heat Transfer Conf., Vol. 5, pp.367-372.

Wallis, G.B., 1969, "*One-Dimensional Two-Phase Flow*," McGraw-Hill, New York.

Wagner, W., 1998, “Wärmeübertragung,” Kamprath Reihe, Vogel Buchverlag, Würzburg.

Wambsganss, M. W., Jendrzejczyk, J. A., France, D. M. and Obot, N. T., 1992, “Frictional Pressure Gradients in Two-Phase Flow in a Small Horizontal Rectangular Channel,” Experimental Thermal and Fluid Science, Vol. 5, pp. 40-56.

Wang, B. X., and Peng X. F., 1994, “Experimental Investigation on Liquid Forced Convection Heat Transfer Through Microchannels,” *Int. J. Heat and Mass Transfer*, Vol. 31, Suppl. 1, pp.73-82.

Yadigaroglu, G., 1981, “Two-Phase Flow Instabilities and Propagation Phenomena,” Thermohydraulics of Two-Phase Systems for Industrial Design and Nuclear Engineering, J.M. Delhay, M. Giot, and M.L. Riethmuller, Eds., pp. 353-403, Hemisphere, Washington, D.C.

Yu, D., Warrington, R., Barron, R. and Ameel, T., 1995, “An Experimental and Theoretical Investigation of Fluid Flow and heat Transfer in Microtubes,” Proceedings, ASME/JSME Thermal Engineering Conference: Vol. 1, pp. 523-530.